AD_____

Award Number: W81XWH-04-1-0697

TITLE: Alpha-v Integrin Targeted PET Imaging of Breast Cancer Angiogenesis and Low-Dose Metronomic Anti-Angiogenic Chemotherapy Efficacy

PRINCIPAL INVESTIGATOR: Xiaoyuan Chen, Ph.D.

CONTRACTING ORGANIZATION: Stanford University School of Medicine
Stanford, CA 94305

REPORT DATE: August 2008

TYPE OF REPORT: Addendum to final report

PREPARED FOR: U.S. Army Medical Research and Materiel Command
Fort Detrick, Maryland 21702-5012

DISTRIBUTION STATEMENT: Approved for Public Release;
Distribution Unlimited

The views, opinions and/or findings contained in this report are those of the author(s) and should not be construed as an official Department of the Army position, policy or decision unless so designated by other documentation.

REPORT DOCUMENTATION PAGE

Form Approved
OMB No. 0704-0188

1. REPORT DATE	2. REPORT TYPE	3. DATES COVERED
August 2008	Addendum to final report	15 July 2007-14 July 2008

4. TITLE AND SUBTITLE

Alpha-v Integrin Targeted PET Imaging of Breast Cancer Angiogenesis and Low-Dose Metronomic Anti-Angiogenic Chemotherapy Efficacy

5a. CONTRACT NUMBER

5b. GRANT NUMBER
W81XWH-04-01-0697

5c. PROGRAM ELEMENT NUMBER

6. AUTHOR(S)

Xiaoyuan Chen, Ph.D.

E-Mail: shawn.chen@nih.gov

5d. PROJECT NUMBER

5e. TASK NUMBER

5f. WORK UNIT NUMBER

7. PERFORMING ORGANIZATION NAME(S) AND ADDRESS(ES)

Stanford University School of Medicine
Stanford, CA 94305

8. PERFORMING ORGANIZATION REPORT NUMBER

9. SPONSORING / MONITORING AGENCY NAME(S) AND ADDRESS(ES)
U.S. Army Medical Research and Materiel Command
Fort Detrick, Maryland 21702-5012

10. SPONSOR/MONITOR'S ACRONYM(S)

11. SPONSOR/MONITOR'S REPORT NUMBER(S)

12. DISTRIBUTION / AVAILABILITY STATEMENT
Approved for Public Release; Distribution Unlimited

13. SUPPLEMENTARY NOTES

14. ABSTRACT

The overall objective of this project is to develop 18F-labeled RGD peptide derivatives for breast cancer imaging with prolonged tumor retention and improved in vivo kinetics to visualize and quantify αv-integrin expression and subsequently evaluate the metronomic antiangiogenic chemotherapy efficacy on tumor regression, necrosis, and angiogenesis. Specific Aims: (1) To optimize 18F-labeled RGD peptide tracer for breast cancer imaging with prolonged tumor retention and improved in vivo kinetics. (2) To demonstrate the feasibility of PET/18F-RGD to image breast tumor growth, spread, and angiogenesis as well as quantifying αv-integrin expression level during breast tumor neovascularization over time. (3) To evaluate the efficacy of EMD 121974/paclitaxel combination on tumor regression, necrosis, and angiogenesis and demonstrate the feasibility of PET/18F-RGD to monitor the treatment outcomes. Major findings: We have developed a series of novel multimeric RGD peptides for PET imaging. We have also successfully demonstrated that suitably labeled RGD peptide allows quantification of integrin expression in vivo in a non-invasive manner. We have also synthesized a RGD-paclitaxel conjugate for breast cancer integrin targeted therapy. Furthermore, RGD peptide-based PET tracer allows early prediction of response to anti-cancer therapeutics including paclitaxtel derivatives.

15. SUBJECT TERMS

16. SECURITY CLASSIFICATION OF:			17. LIMITATION OF ABSTRACT	18. NUMBER OF PAGES	19a. NAME OF RESPONSIBLE PERSON USAMRMC
a. REPORT	**b. ABSTRACT**	**c. THIS PAGE**	UU		**19b. TELEPHONE NUMBER** *(include area code)*
U	U	U			

Table of Contents

Introduction

During the no-cost extension period (August 2007 to December 2007), we published the results of using RGD peptide paclitaxel conjugate to treat breast cancer. We also applied suitably labeled RGD peptide tracers to monitor breast cancer response to Abraxane therapy.

Body

During the no-cost extension period (August 2007 to December 2007). The research work titled "Evaluation of biodistribution and anti-tumor effect of a dimeric RGD peptide-paclitaxel conjugate in mice with breast cancer" was published in *Eur J Nucl Med Mol Imaging* 2008;35(8):1489-98 (PMID: 18373091).

More recently we also applied integrin imaging to follow the early response to Abraxane therapy. Abraxane (nanoparticle albumin-bound paclitaxel) is an anticancer drug approved by the Food and Drug Administration. However, the mechanism of action of Abraxane is complex, and no established biomarker is available to accurately monitor its treatment outcomes. Orthotopic MDA-MB-435 breast cancer mice were treated with Abraxane (25 mg/kg every other day, 3 doses) or phosphate-buffered saline. Tumor volume was monitored by caliper measurement. PET scans were obtained before and at different times after the start of treatment (days 0, 3, 7, 14, and 21) using ^{18}F-FPPRGD2 and ^{18}F-FDG. The tumoricidal effect was also assessed ex vivo by immunohistochemistry. Abraxane treatment inhibited the tumor growth, and a significant difference in tumor volume could be seen at day 5 after the initiation of treatment. The tumor uptake of ^{18}F-FPPRGD2 in the Abraxane-treated group was significantly lower on days 3 and 7 than at baseline but returned to the baseline level at days 14 and 21, indicative of relapse of the tumors after the treatment was halted. Immunohistologic staining confirmed that the change of ^{18}F-FPPRGD2 uptake correlated with the variation of integrin level in the tumor vasculature induced by Abraxane treatment. No significant change of tumor (rather than vascular) integrin expression was observed throughout the study. No significant decrease of ^{18}F-FDG uptake was found between the treated and the control tumors on days 3, 14, and 21, although an increase in ^{18}F-FDG tumor uptake of treated mice, as compared with the control mice, was found on day 7. The increase of ^{18}F-FDG on day 7 was related to the inflammatory response during therapy. Abraxane-mediated downregulation of integrin $\alpha v\beta 3$ expression on tumor endothelial cells can be quantitatively visualized by PET. The change of integrin expression precedes that of tumor size. Consequently, ^{18}F-FPPRGD2 PET is superior to ^{18}F-FDG PET in monitoring early response to treatment, favoring its potential clinical translation. This work was published in *J Nucl Med* 2011;52(1):140-6 (PMID: 21149494) . The erratum was published in *J Nucl Med* 2012;53(11):1824.

Key Research Accomplishments

- Developed RGD-drug conjugate for improve tumor delivery and anticancer effect as compared to the chemotherapeutic drug without conjugation;
- Developed a novel PET tracer ^{18}F-FPPRGD2 for imaging integrin $\alpha v\beta 3$ level;
- Applied ^{18}F-FPPRGD2 and ^{18}F-FDG to monitor anticancer treatment;

Reportable Outcomes

Cao Q, Li ZB, Chen K, Wu Z, He L, Neamati N, Chen X.
Evaluation of biodistribution and anti-tumor effect of a dimeric RGD peptide-paclitaxel conjugate in mice with breast cancer.
Eur J Nucl Med Mol Imaging. 2008 Aug;35(8):1489-98. doi: 10.1007/s00259-008-0744-y. Epub 2008 Mar 29.

Sun X, Yan Y, Liu S, Cao Q, Yang M, Neamati N, Shen B, Niu G, Chen X.
^{18}F-FPPRGD2 and ^{18}F-FDG PET of response to Abraxane therapy.
J Nucl Med. 2011 Jan;52(1):140-6. doi: 10.2967/jnumed.110.080606. Epub 2010 Dec 13.

Conclusion

- ^{18}F-FPPRGD2 is a promising PET tracer that allows noninvasive evaluation of response to treatments that affect integrin αvβ3 level, before size changes can be found.
- ^{18}F-FPPRGD2 also has the potential to provide earlier clinical opportunities to adjust anticancer drug doses and intervals to maintain sustained antitumor effect and avoid relapse.
- ^{18}F-FPPRGD2 is superior to ^{18}F-FDG in monitoring anticancer treatment, because ^{18}F-FPPRGD2 imaging is not significantly affected by the presence of infiltrating macrophages in regressing tumors.

References

None.

Appendices

Reprint: Eur J Nucl Med Mol Imaging. 2008 Aug;35(8):1489-98.

Reprint: J Nucl Med. 2011 Jan;52(1):140-6.

ORIGINAL ARTICLE

Evaluation of biodistribution and anti-tumor effect of a dimeric RGD peptide–paclitaxel conjugate in mice with breast cancer

**Qizhen Cao · Zi-Bo Li · Kai Chen · Zhanhong Wu ·
Lina He · Nouri Neamati · Xiaoyuan Chen**

Abstract

Purpose Targeting drugs to receptors involved in tumor angiogenesis has been demonstrated as a novel and promising approach to improve cancer treatment. In this study, we evaluated the anti-tumor efficacy of a dimeric RGD peptide–paclitaxel conjugate (RGD2–PTX) in an orthotopic MDA-MB-435 breast cancer model.
Methods To assess the effect of conjugation and the presence of drug moiety on the MDA-MB-435 tumor and normal tissue uptake, the biodistribution of ^{3}H–RGD2–PTX was compared with that of ^{3}H–PTX. The treatment effect of RGD2–PTX and RGD2+PTX was measured by tumor size, ^{18}F-FDG/PET, ^{18}F-FLT/PET, and postmortem histopathology.
Results By comparing the biodistribution of ^{3}H–RGD2–PTX and ^{3}H–PTX, we found that ^{3}H–RGD2–PTX had higher initial tumor exposure dose and prolonged tumor retention than ^{3}H–PTX. Metronomic low-dose treatment of breast cancer indicated that RGD2–PTX is significantly more effective than PTX+RGD2 combination and solvent control. Although in vivo ^{18}F-FLT/PET imaging and ex vivo Ki67 staining indicated little effect of the PTX-based drug on cell proliferation, ^{18}F-FDG/PET imaging showed significantly reduced tumor metabolism in the RGD2–PTX-

treated mice versus those treated with RGD2+PTX and solvent control. Terminal uridine deoxynucleotidyl transferase dUTP nick-end labeling (TUNEL) staining also showed that RGD2–PTX treatment also had significantly higher cell apoptosis ratio than the other two groups. Moreover, the microvessel density was significantly reduced after RGD2–PTX treatment as determined by CD31 staining.
Conclusion Our results demonstrate that integrin-targeted delivery of paclitaxel allows preferential cytotoxicity to integrin-expressing tumor cells and tumor vasculature. The targeted delivery strategies developed in this study may also be applied to other chemotherapeutics for selective tumor killing.

Q. Cao · Z.-B. Li · K. Chen · Z. Wu · L. He · X. Chen (✉)
The Molecular Imaging Program at Stanford (MIPS),
Department of Radiology, Biophysics, and Bio-X Program,
Stanford University School of Medicine,
1201 Welch Rd,
Stanford P095, CA 94305-5484, USA
e-mail: shawchen@stanford.edu

N. Neamati
Department of Pharmacology and Pharmaceutical Sciences,
University of Southern California, School of Pharmacy,
Los Angeles, CA, USA

Introduction

Paclitaxel (Taxol, PTX), a complex taxane diterpene, was originally isolated from *Taxus brevifolia* as a potent anti-tumor agent [1]. It binds and stabilizes β-tubulin in the microtubules [2, 3] and thereby represses dynamic instability, causing the formation of parallel bundles of micro-tubules and inhibiting cell division at the G2-M phase of the cell cycle [3–5]. Due to its significant anti-tumor activity, PTX has been commonly used in the treatment of ovarian, breast, head and neck cancer, and Kaposi's sarcoma [6–9]. However, the use of PTX is limited by the drug's toxicity (i.e., acute myelosuppression and peripheral neurotoxicity) and extremely low aqueous solubility. To increase the therapeutic index, various drug delivery

🙌 Springer

systems are being developed, which includes the use of liposomes [10], microspheres [11], micelles [12], prodrugs [13, 14], and polymer–drug conjugates [15].

Recently, the development of target-specific agents has proven to be an efficient method for improving tumor selectivity of anti-cancer drugs [16, 17]. Tumor-selective approach targets specific receptors or other markers that are overexpressed on the surface of tumor cells. The cell adhesion molecule integrin $\alpha_v\beta_3$ is not readily detectable in quiescent vessels but becomes highly expressed in angiogenic vessels and tumor cells [18]. This restricted expression profile and good accessibility of integrin $\alpha_v\beta_3$ make it an ideal target for drug delivery purposes [19]. Synthetic peptides containing the arginine–glycine–aspartate (RGD) motif could specifically interact with integrin $\alpha_v\beta_3$, making them suitable for integrin $\alpha_v\beta_3$-targeted delivery.

We have previously conjugated PTX with a dimeric RGD peptide E[c(RGDyK)]$_2$ (Fig. 1) and evaluated the anti-tumor activity in a metastatic breast cancer cell line MDA-MB-435 [17]. The in vitro results showed that the RGD2–PTX conjugate inhibited cell proliferation with activity comparable to that observed for paclitaxel, both of which were mediated by an arrest of G2/M phase of the cell cycle followed by apoptosis. In addition, when RGD2–PTX was labeled with ^{125}I through the tyrosine residue on the RGD peptide, integrin-specific accumulation of ^{125}I–RGD2–PTX in orthotopic MDA-MB-435 tumor was observed. In this study, we would like to extend this effort and study the anti-tumor effect of RGD2–PTX in vivo.

Materials and methods

All reagents, unless otherwise specified, were of analytical grade and purchased commercially. Dimeric RGD peptide E[c(RGDyK)]$_2$ was synthesized by Peptides International, Inc (Louisville, KY, USA). PTX-2′-succinate (PTXSX) was prepared by reacting PTX (Hande Tech, Houston, TX, USA) with equal molar amount of succinic anhydride in pyridine [20]. ^{3}H–PTX was purchased from Moravek Biochemicals, Inc. (Brea, CA, USA) with a specific activity of 2.4 Ci/mmol.

Preparation of RGD2–PTX and ^{3}H–RGD2–PTX conjugate

RGD2-PTX was prepared from dimeric RGD peptide E[c (RGDyK)]$_2$ according to our previously reported procedure [17]. ^{3}H–RGD2–PTX was also obtained by using the same method. In brief, ^{3}H–PTX was mixed with excess amount of non-radioactive PTX and reacted with succinate anhydride to provide carrier-added ^{3}H-PTXSX. The active ester ^{3}H-PTXSX-OSSu was then prepared in situ and added to a solution of dimeric RGD peptide. The reaction mixture was incubated at 4°C overnight and then purified by semi-preparative reversed-phase high-performance liquid chromatography (RP-HPLC) on a Dionex 680 chromatography system with a UVD 170U absorbance detector. After lyophilization, ^{3}H–RGD2–PTX conjugate was obtained as white fluffy powder in 48% yield with specific activity of 1.68 μCi/mg.

Fig. 1 Chemical structures of PTX and RGD2–PTX conjugate
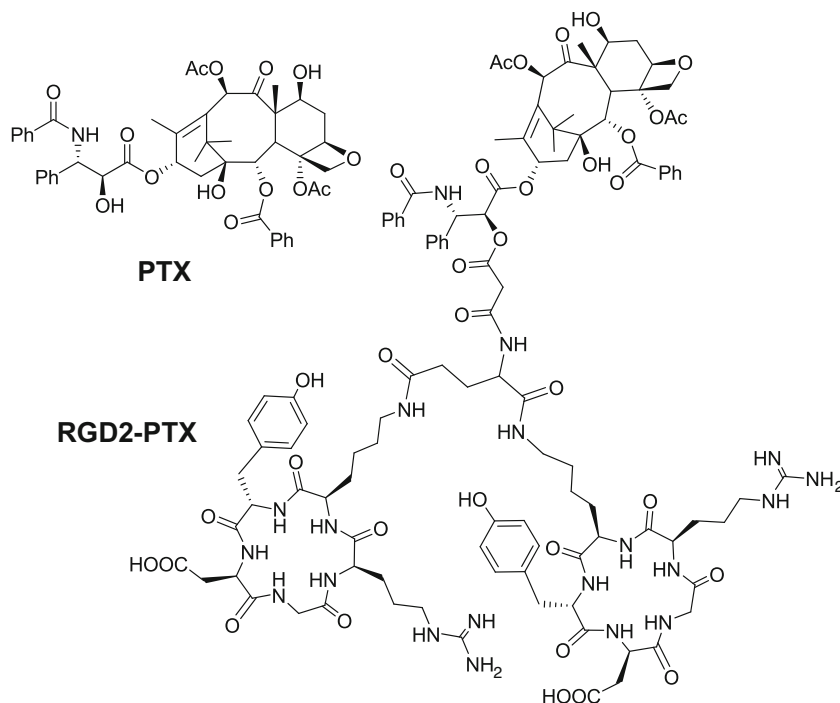
Animal model

All animal experiments were performed in compliance with the guidelines for the care and use of research animals established by the Stanford University's Animal Studies Committee. Female athymic nude mice (*nu/nu*) were obtained from Harlan (Indianapolis, IN, USA) at 6–8 weeks of age and were kept under sterile conditions. The MDA-MB-435 cells were harvested and suspended in sterile phosphate-buffered saline (PBS) at a concentration of 5×10^7 cells/ml. Viable cells (5×10^6) in PBS (100 μl) were injected orthotopically in the right mammary fat pad. Palpable tumors appeared by day 10–14 post-implantation. Tumor growth was followed by caliper measurements of perpendicular measures of the tumor. The tumor volume was estimated by the formula: tumor volume $=a\times(b^2)/2$, where *a* and *b* are the tumor length and width, respectively, in millimeters.

Biodistribution

To assess the effect of conjugation and the presence of drug moiety on the MDA-MB-435 tumor and normal tissue uptake, the biodistribution of ^{3}H–RGD2–PTX was compared with that of ^{3}H–PTX. Orthotopic MDA-MB-435 tumor-bearing female athymic nude mice (*n*=3 per time point) were injected with 2.9 μmol/kg ^{3}H–RGD2–PTX or ^{3}H–PTX via the tail vein. The animals were euthanized at 4, 24, and 48 h post-injection, and major organs and tissues were collected correspondingly. Approximately 100 mg of the tissue was added to glass scintillation vials containing 1 ml of tissue solubilizer SoluEne®-350 (Perkin-Elmer, Waltham, MA, USA). These samples were digested at 55°C overnight followed by bleaching to obtain the decolorized samples. Chemiluminescence was reduced by the addition of glacial acetic acid. Hionic-Fluor liquid scintillation cocktail (Perkin-Elmer) was added to all samples, which were then counted with a Tri-Carb 2800TR liquid scintillation analyzer (Perkin-Elmer).

Treatment of MDA-MB-435 breast cancer model

When palpable tumors were present in all animals (100–150 mm^3), mice were randomly divided into three groups (*n*=8 per group). Groups 1 and 2 were treated with solvent control [10% dimethyl sulphoxide (DMSO)/90% normal saline] and 15 mg/kg RGD+10 mg/kg PTX mixture, respectively. Group 3 was treated with 25 mg/kg RGD2–PTX conjugates to keep the effective PTX dose at the same level as group 2 (10 mg/kg PTX motif). Each mouse was treated by i.p. injection every 3 days with a total of five doses. The mouse body weight and tumor volume were measured every 3 days for up to 20 days before euthanasia.

MicroPET imaging

Detailed procedure for positron emission tomography (PET) imaging has been reported earlier [21]. Briefly, PET scans were performed using a microPET R4 rodent model scanner (Siemens Medical Solutions). After 6 h fasting, mice were injected with about 100 μCi of 2-deoxy-2-[^{18}F]fluoro-D-glucose (^{18}F-FDG) or 3′-deoxy-3′-[^{18}F]-fluorothymidine (^{18}F-FLT) via tail vein under isoflurane anesthesia, and 3–5 min PET scans were performed at 1 h post-injection (p.i.). The images were reconstructed by a two-dimensional ordered subsets expectation maximum algorithm with no attenuation or scatter correction. For each microPET scan, regions of interest (ROIs) were drawn over the tumor by using vendor software ASI Pro 5.2.4.0 on decay-corrected whole-body coronal images. Assuming a tissue density of 1 g/ml, the ROIs were converted to MBq/g per min using a conversion factor and then divided by the administered activity to obtain an imaging ROI-derived percent injected dose per gram (% ID/g).

Double staining of TUNEL and human integrin $\alpha_v\beta_3$

Frozen tissue slices (5-μm thick) were taken out from freezer and warmed for 20 min at room temperature. Fluorescent TUNEL assay was then conducted by following the manual instruction of In Situ Cell Death Detection kit (Roche, Indianapolis, IN, USA). After TUNEL staining, slides were blocked with 10% goat serum in PBS for 15 min at room temperature and incubated with anti-human $\alpha_v\beta_3$ antibody (MedImmune, Gaithersburg, MD, USA) for 1 h at room temperature. After 3×5 min washing with PBS, slides were incubated with flourescein isothiocyanate (FITC)-conjugated goat anti-human secondary antibody (Jackson ImmunoResearch Laboratories, Inc., West Grove, PA, USA). After staining, slides were mounted with Vectashield mounting medium (Vector Laboratories, Buringame, CA, USA) and examined under an epifluorescence microscope (Carl Zeiss Axiovert 200 M).

Ki67 and CD31 immunofluorescence staining

Frozen tumor sections (5-μm thick) were fixed with cold acetone for 10 min and dried in the air for 30 min. After blocking with 10% donkey serum for 30 min at room temperature, the sections were incubated with rabbit anti-human Ki67 (1:100, NeoMarkers, Fremont, CA, USA) or rat anti-mouse CD31 antibodies (1:100, BD Biosciences, San Jose, CA, USA) separately overnight at 4°C. After incubation with Cy3-conjugated donkey anti-rabbit and Cy3-conjugated donkey anti-rat secondary antibodies (1:200, Jackson ImmunoResearch Laboratories, Inc.), the slides were mounted with 4′,6-diamidino-2-phenylindole

(DAPI)-containing mounting medium and examined under an epifluorescence microscope (Carl Zeiss Axiovert 200 M).

Statistical analysis

Statistical significance was determined by one-way ANOVA using the computer Statistical Package for the Social Sciences (SPSS; 10.0) statistic package. P value< 0.05 was considered significant.

Result

Chemistry and radiochemistry

The synthesis of RGD2–PTX was performed through an active ester method. PTX-SX was activated and then conjugated with the amino group of dimeric RGD peptide under a slightly basic condition. RGD2–PTX was obtained as a fluffy white powder [17]. ^{3}H–RGD2–PTX was synthesized by the same method. However, non-radioactive PTX was added as a carrier to improve the yield. Although the specific activity of ^{3}H–RGD2–PTX was dropped to 1.68 μCi/mg, it is still sufficient for the following biodistribution studies.

Biodistribution of ^{3}H–PTX and ^{3}H–RGD2–PTX

[3]H–PTX and ^{3}H–RGD2–PTX were injected at equivalent molar amount to guarantee the comparability. As seen from Table 1, the highest concentration of ^{3}H–PTX was found in the liver at 4 h (2389.3±408.8 ng/g). No significant difference was observed for the accumulation of ^{3}H–PTX

between the muscle (257.3±32.2 ng/g) and the tumor (239.0±56.2 ng/g). The ^{3}H–PTX also cleared very fast from the body. As compared with the 4 h time point, the concentration of ^{3}H–PTX at 24 h dropped by 20-fold in the liver (123.4±12.2 ng/g) and ninefold in kidneys (38.0± 13.3 ng/g). Such low levels were maintained throughout 48 h. We also observed around threefold decrease for the concentration of ^{3}H–PTX in the tumor at 24 h (85.6± 15.2 ng/g) as compared to that at 4 h (239.0±56.2 ng/g), which was further reduced to 45.8±1.69 ng/g (5.2-fold decrease compared with 4 h time point) at 48 h post-drug administration. The tumor/muscle ratio was determined to be 0.93 at 4 h, 2.08 at 24 h, and 1.29 at 48 h.

In contrast, ^{3}H–RGD2–PTX had a tumor uptake of 357.5±62.62 ng/g effective PTX concentration at 4 h, 229.4±50.4 ng/g at 24 h, and 148.8±40.2 ng/g at 48 h time point (Table 2). The tumor uptake of ^{3}H–RGD2–PTX in MDA-MB-435 tumor is significantly higher than ^{3}H–PTX at all time points examined ($P<0.001$), and the tumor clearance rate is also much slower, presumably due to integrin-specific delivery of PTX based on our previous experiments [17]. The muscle uptake of ^{3}H–RGD2–PTX was also lower than ^{3}H–PTX. The resulting tumor-to-muscle ratios of ^{3}H–RGD2–PTX were 2.86 at 4 h, 2.82 at 24 h, and 1.74 at 48 h, which were significantly higher than those of ^{3}H–PTX ($P<0.05$). It is of note that the initial liver uptake of ^{3}H–RGD2–PTX (1,252.9±109.9 ng/g at 4 h) was significantly lower than that of ^{3}H–PTX ($P<0.01$). However, ^{3}H–PTX tends to clear faster than ^{3}H–RGD2–PTX. Renal uptake of ^{3}H–RGD2–PTX is higher than ^{3}H–PTX ($P<0.01$) at both early and late time points, which may be attributed to both renal clearance and integrin-specific binding of RGD2–PTX, as the endothelial cells of small

Table 1 Tissue distribution of ^{3}H–PTX in Balb/c nude mice bearing MDA-MB-435 tumor

Organ	4 h	24 h	48 h
Blood	67.1±9.8	42.7±14.7	35.0±1.5
Skin	135.1±23.5	24.6±3.2	25.4±9.3
Muscle	257.3±32.2	41.1±17.2	35.4±10.7
Heart	200.7±48.5	37.2±10.7	42.9±10.9
Lung	329.2±18.2	35.2±5.4	47.9±8.8
Liver	2389.3±408.8	123.4±12.2	132.6±31.9
Kidney	339.6±67.6	38.0±13.3	35.7±2.0
Spleen	365.5±118.5	51.6±7.6	36.4±8.4
Stomach	180.7±15.7	24.4±4.7	17.2±4.0
Intestine	274.1±110.1	14.4±2.5	12.8±7.0
Tumor	239.0±56.2	85.6±15.2	45.8±1.7
Tumor/muscle	0.93	2.08	1.29
Tumor/liver	0.1	0.69	0.34
Tumor/kidney	0.7	2.25	1.28

Values are mean ± SD (n=3) and shown as ^{3}H–PTX concentration (ng/g tissue).

Table 2 Tissue distribution of ^{3}H–RGD2–PTX in Balb/c nude mice bearing MDA-MB-435 tumor

Organ	4 h	24 h	48 h
Blood	101.7±30.8	143.1±18.0	225.4±12.8
Skin	144.1±15.9	87.2±16.1	66.0±9.1
Muscle	125.1±24.0	81.2±11.4	85.6±28.0
Heart	228.7±29.8	170.7±18.6	222.5±16.2
Lung	300.4±30.9	238.6±75.6	207.8±48.2
Liver	1252.9±109.9	510.4±28.9	545.3±30.6
Kidney	1421.6±289.8	338.9±22.1	281.8±32.6
Spleen	322.3±59.3	228.7±39.4	227.9±28.2
Stomach	119.0±16.7	71.63±9.5	71.7±12.2
Intestine	127.8±20.3	52.1±7.5	50.8±9.5
Tumor	357.5±62.6	229.4±50.4	148.8±40.2
Tumor/muscle	2.86	2.82	1.74
Tumor/liver	0.29	0.45	0.27
Tumor/kidney	0.25	0.68	0.53

Values are mean ± SD (n=3) and shown as ^{3}H–RGD2–PTX concentration (ng/g tissue).

glomerulus vessels of rodent kidneys express β_3 integrin. Also note that the blood activity for ^{3}H–RGD2–PTX was considerably higher than ^{3}H–PTX, which might be related to the metabolic instability of the construct. Overall, prominent tumor uptake and retention of RGD2–PTX may provide tumor treatment benefit over PTX.

Treatment of MDA-MB-435 breast cancer model

To determine whether RGD2–PTX conjugate has better anti-tumor effect than the combination of PTX+RGD2 (in equal PTX dose) in vivo as we proposed, female athymic nude mice bearing MDA-MB-435 tumor were randomly divided into three groups and treated with vehicle (saline with 10% DMSO), RGD2 (15 mg/kg) plus PTX (10 mg/kg), or RGD2–PTX conjugate 25 mg/kg (equimolar dose of PTX) every 3 days (a total of five doses). As shown in Fig. 2a, the combination of RGD2 plus PTX therapy started to show significant therapeutic effect as compared with the vehicle control group at day 15 when the treatment was initiated ($P<0.05$). However, the effectiveness of RGD2–PTX conjugate treatment became obvious as compared to the other two treatments after two doses. After day 9, RGD2–PTX conjugate group showed even more tumor suppression effect ($P<0.01$ compared with the vehicle group; $P<0.05$ compared with the PTX+RGD2 group). Moreover, no significant body weight difference was observed among these three treatment groups (Fig. 2b).

^{18}F-FDG and ^{18}F-FLT microPET imaging

^{18}F-FDG microPET is a functional imaging technique that reflects the glycolytic rate of tissues and has been used to measure the increased metabolic demand in tumor cells.

Currently, the use of PET for response assessment is changing from evaluation at the end of treatment to prediction of tumor response early during the course of therapy. Therefore, we performed ^{18}F-FDG microPET on day 10 after three doses of treatment. As shown in Fig. 3a, b, the tumor uptake of ^{18}F-FDG was decreased from 7.95 ± 0.39%ID/g (vehicle control group) to 6.73 ± 0.50%ID/g in PTX+RGD2 treatment group and to 5.97 ± 0.54%ID/g in the RGD2–PTX treatment group ($P<0.01$). These tumor uptakes during the treatment correlated well with our therapy results at later time points. To assess the effects of therapy on tumor proliferation, ^{18}F-FLT imaging [22] was also conducted. No significant difference was observed among the control and two treatment groups ($P>0.05$, Fig. 3c,d). In fact, the tumor growth curve showed a steady increase of tumor growth in all three groups, which may also suggest that the PTX could not effectively inhibit cell proliferation in this experiment.

Immunofluorescence staining

To evaluate whether cell apoptosis was involved in the RGD2–PTX-enhanced regression on MDA-MB-435 tumors, the TUNEL assay was used to quantify cell apoptosis in tumor sections from all three groups. As shown in Fig. 4, vehicle-treated tumors did not show specific cell apoptosis. Combination of RGD2 with PTX for the treatment only resulted in moderately positive TUNEL staining at the tumor peripheral area. In contrast, RGD2–PTX conjugate treatment group showed significant cell apoptosis throughout the tumor. At the same time, we also detected human integrin $\alpha_v\beta_3$ expression on the same tissue section by immunofluorescence staining. Although TUNEL staining was quite different among these three
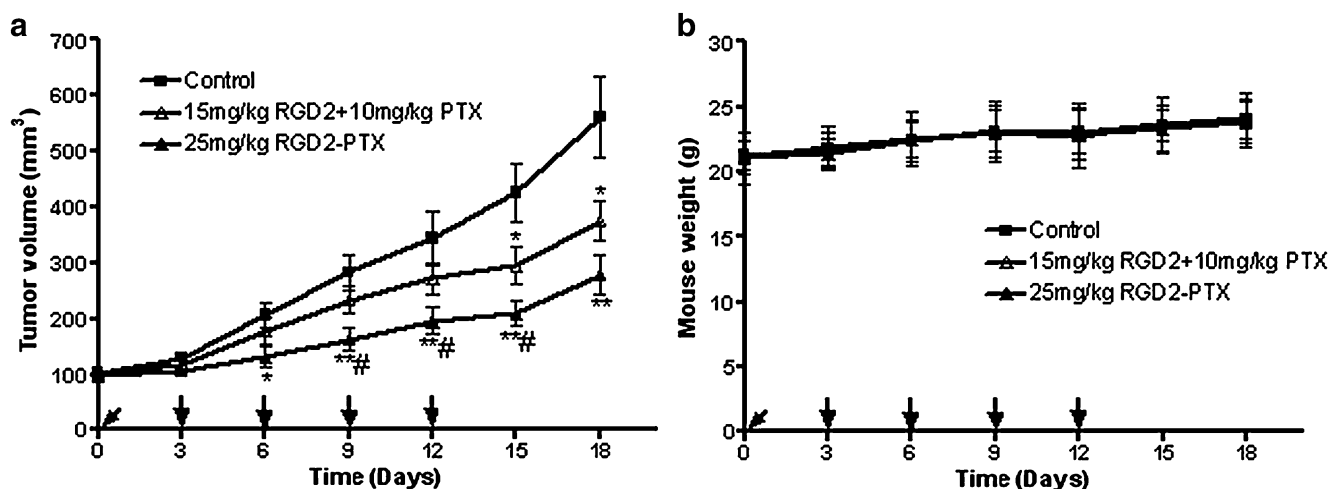

Fig. 2 a Effect of solvent only, RGD2+PTX, and RGD2-PTX treatment on the growth of MDA-MB-435 breast cancer model. Averaged tumor size was monitored every 3 days and shown as mean ± SE ($n=8$ per group). b The mice weight of the control group or treatment group over time ($n=8$ per group). The drug administration intervals were indicated by *arrows*, where * or # denotes $P<0.05$ and **$P<0.01$. *Single and double asterisks*, compared with the solvent control group; *number sign*, compared with the RGD2+PTX treatment group
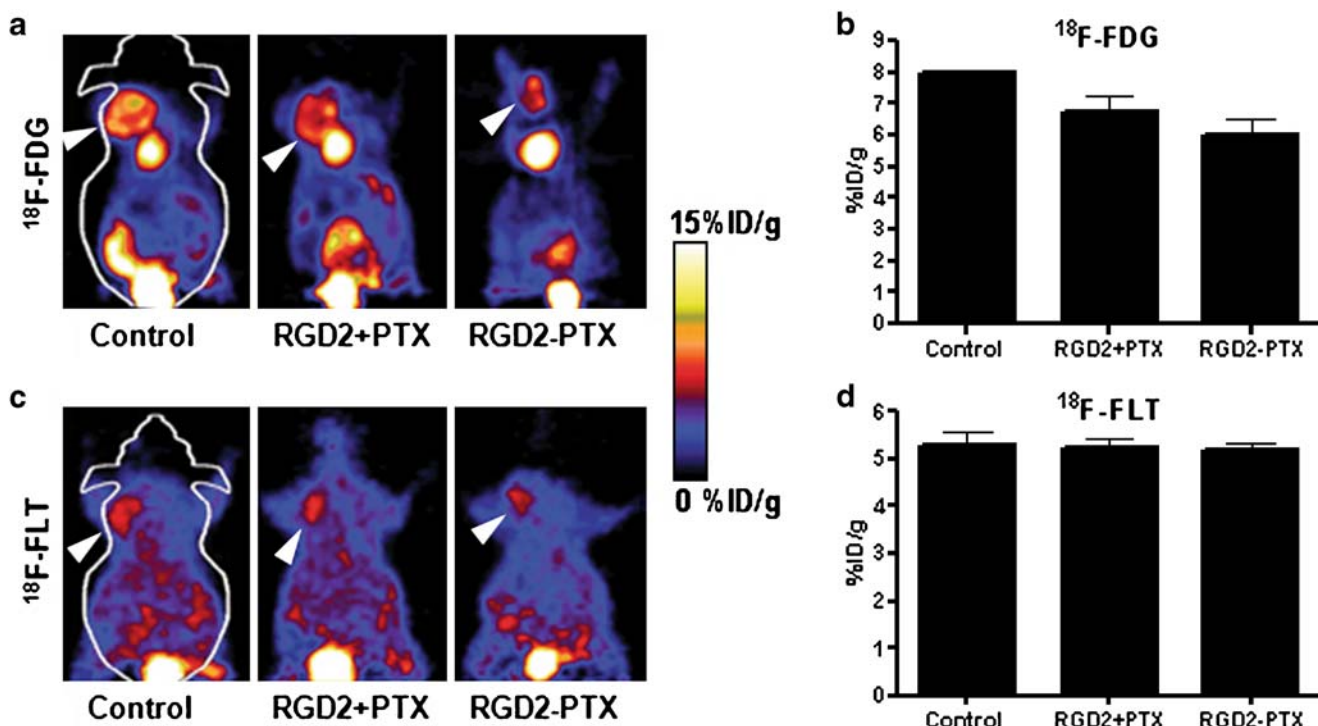
Fig. 3 **a** Representative whole-body coronal microPET images of MDA-MB-435 tumor-bearing mice with ^{18}F-FDG at day 10 during the therapy. **b** Comparison between the uptake of ^{18}F-FDG in MDA-MB-435 tumor with solvent treatment only, RGD2+PTX, or RGD2-PTX. Regions of interest (ROIs) were shown as % ID/g ± SD ($n=3$/group). **c** Representative whole-body coronal microPET images of MDA-MB-435 tumor-bearing mice with ^{18}F-FLT at day 11 during the therapy. **d** Comparison between the uptake of ^{18}F-FLT in MDA-MB-435 tumors with solvent treatment only, RGD2+PTX or RGD2–PTX. Regions of interest (ROIs) were shown as % ID/g ± SD ($n=3$/group). Tumors were indicated by *arrows*, where *$P<0.05$ and **$P<0.01$
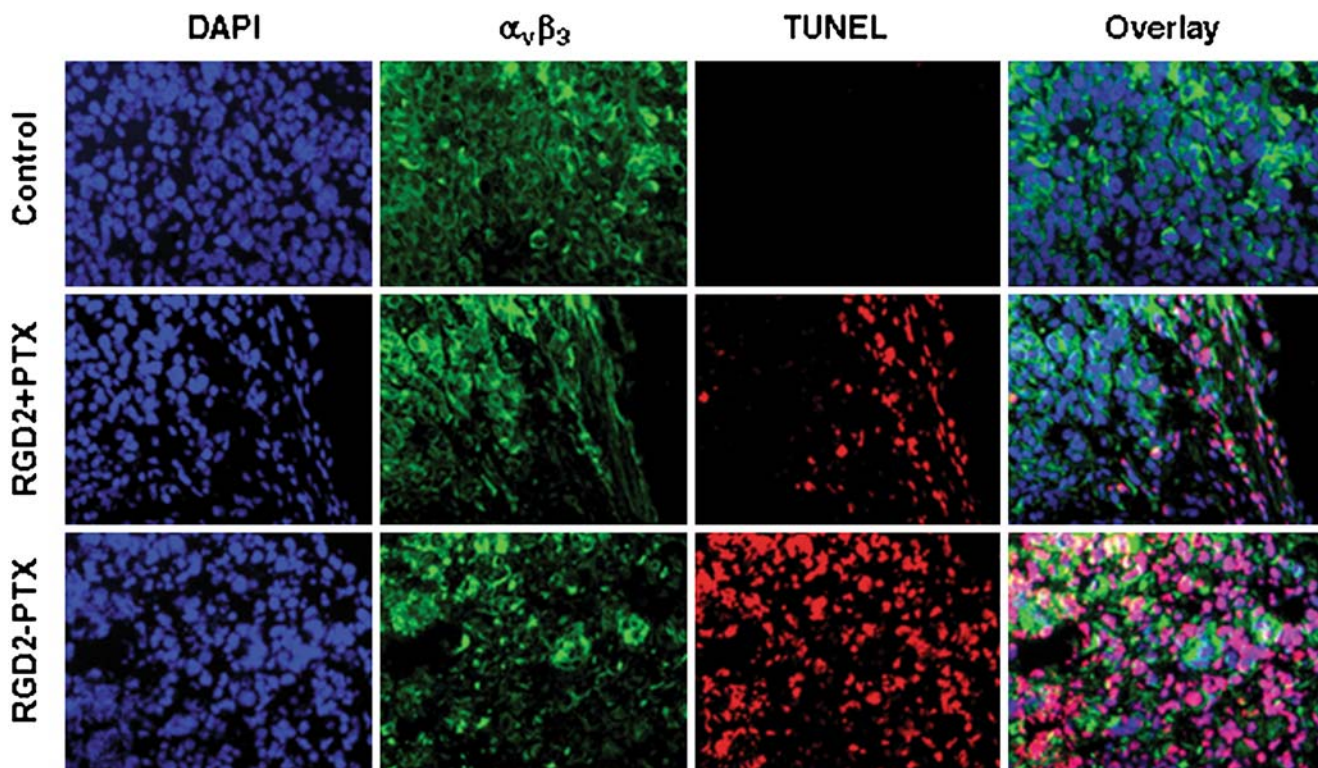

Fig. 4 Immunofluorescence staining of DAPI, human integrin $\alpha_v\beta_3$, TUNEL, and the overlay for MDA-MB-435 tumor tissue from three treatment groups

groups, all tumor sections showed similar integrin $\alpha_v\beta_3$ expression pattern. For the PTX+RGD2 treatment group, PTX seems to be accumulated only on the angiogenic edge of the tumor and cause apoptosis at the corresponding tumor periphery. The center of the tumor with necrosis and low vessel density does not allow efficient diffusion of PTX, and thus little or no PTX-induced apoptosis was observed. For the RGD2–PTX treatment group, TUNEL-positive staining was found throughout the tumor with excellent overlay with integrin $\alpha_v\beta_3$, confirming the effectiveness of integrin-specific delivery of PTX.

We also carried out the CD31 staining to study the effect of PTX treatment on vascular damage. Microvessel density (MVD) analysis revealed that RGD2–PTX-treated tumor had significantly lower vessel density (13.3 ± 5.7 vessels/mm^2) than the PTX+RGD2-treated tumor (24.0 ± 3.2 vessels/mm^2; $P<0.01$, Fig. 5) and the solvent-treated tumor (37.0 ± 8.1 vessels/mm^2; $P<0.01$, Fig. 5). The tumor vessels in the PTX+RGD2 treatment group tend to have large diameters, while the vessels in the RGD2–PTX treatment group tend to be small and irregular. To value whether tumor cell proliferation inhibition was also involved in the RGD2–PTX-enhanced regression on MDA-MB-435 tumors, the Ki67 (cell proliferation marker) immunofluorescence was used to quantify cell proliferation in tumor sections from all groups. However, no significantly delayed cell proliferation was observed in the RGD2–PTX conjugate therapy group compared with the vehicle control group and combination (RGD2+PTX) group

Fig. 5 a Immunofluorescence staining of DAPI, CD31, and the overlay for MDA-MB-435 tumor tissues from three treatment groups. b Microvessel density (MVD) analysis of MDA-MB-435 tumor tissues from three treatment groups ($n=$ 10 per group). Where ** or ## denotes $P<0.01$, ***$P<0.01$. Single and double asterisks, compared with the solvent control group; double number sign, compared with the RGD2+PTX treatment group
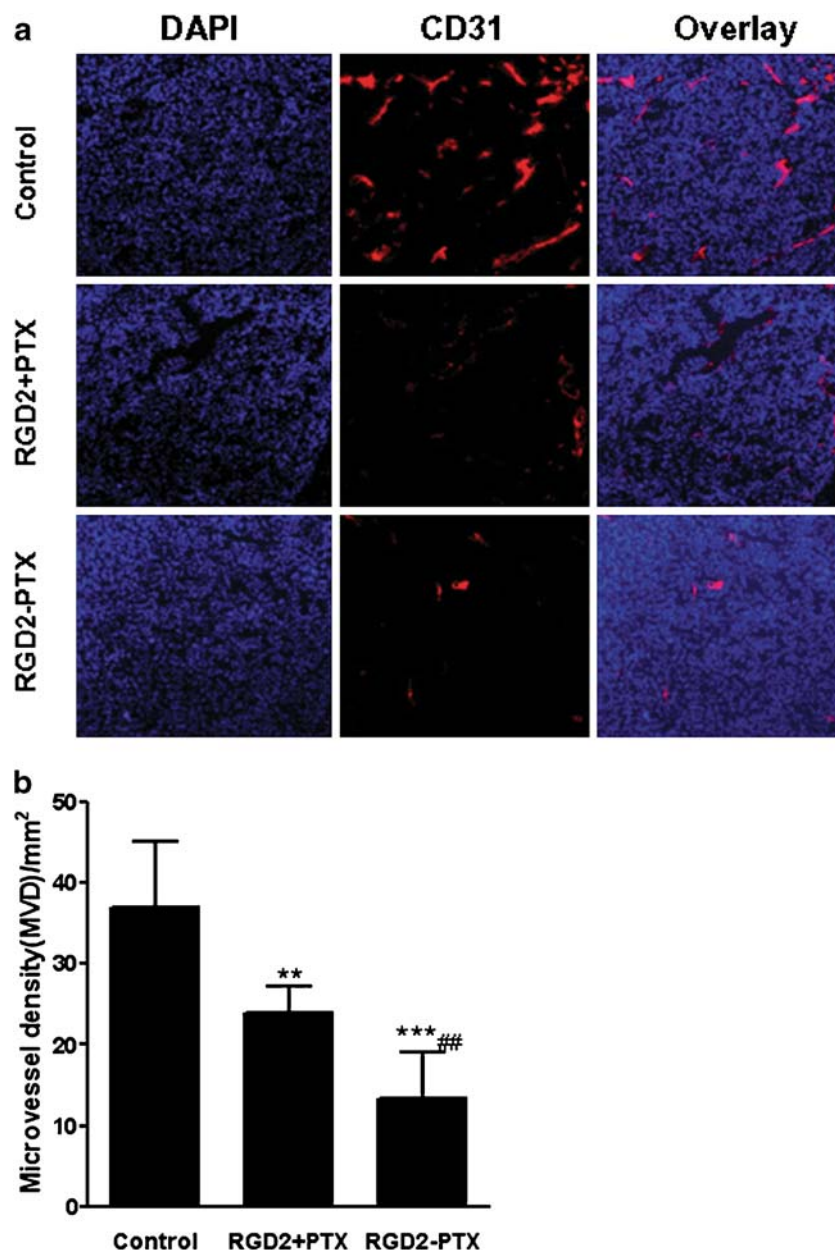
(Fig. 6), which was also consistent with the ^{18}F-FLT imaging result (Fig. 3c,d).

Discussion

The anti-tumor efficacy of clinically used anti-cancer drugs is often limited by their non-specific toxicity to proliferating normal cells, which could result in low therapeutic index and narrow therapeutic window. Previously, we have demonstrated that targeting drugs to receptors involved in tumor angiogenesis is a novel and promising approach to improve cancer treatment [17]. The RGD2–PTX was constructed from a dimeric RGD peptide E[c(RGDyK)]$_2$ and PTX through the 2′-hydroxy group of paclitaxel and the amino group of RGD glutamate residue [17]. A metabolically unstable ester bond is preferred here, as PTX, an anti-microtubule agent, needs to be released from the RGD2–PTX construct once

inside the cell to exert its toxicity. By targeting integrin $\alpha_v\beta_3$ through the RGD motif, improved tumor specificity and cytotoxic effect of paclitaxel was observed. In this work, we evaluated the tumor therapeutic effect of RGD2–PTX in vivo in comparison with PTX+RGD2 treatment and solvent-only treatment.

Although we have synthesized ^{125}I–RGD2–PTX and studied its distribution in vivo, the ^{125}I was labeled to RGD motif, and the ester bond between RGD2 and PTX was metabolically unstable. Once the ester bond is broken, ^{125}I counting would only reflect the distribution of dimeric RGD instead of PTX. Therefore, we studied the distribution of ^{3}H–RGD2–PTX, which is more relevant to the pharmacokinetics of PTX within RGD2–PTX. Our experimental results in vivo showed that ^{3}H–RGD2–PTX conjugate possessed higher tumor uptake and prolonged tumor retention than ^{3}H–PTX, which may count for the better therapeutic efficacy of RGD2–PTX than RGD2+PTX.

Fig. 6 a Immunofluorescence staining of Ki67, DAPI, and the overlay for MDA-MB-435 tumor tissues from the control, RGD2+PTX, and RGD2-PTX treatment groups. **b** Ki67-positive cell counting showed little or no difference among three treatment groups ($P>0.05$)
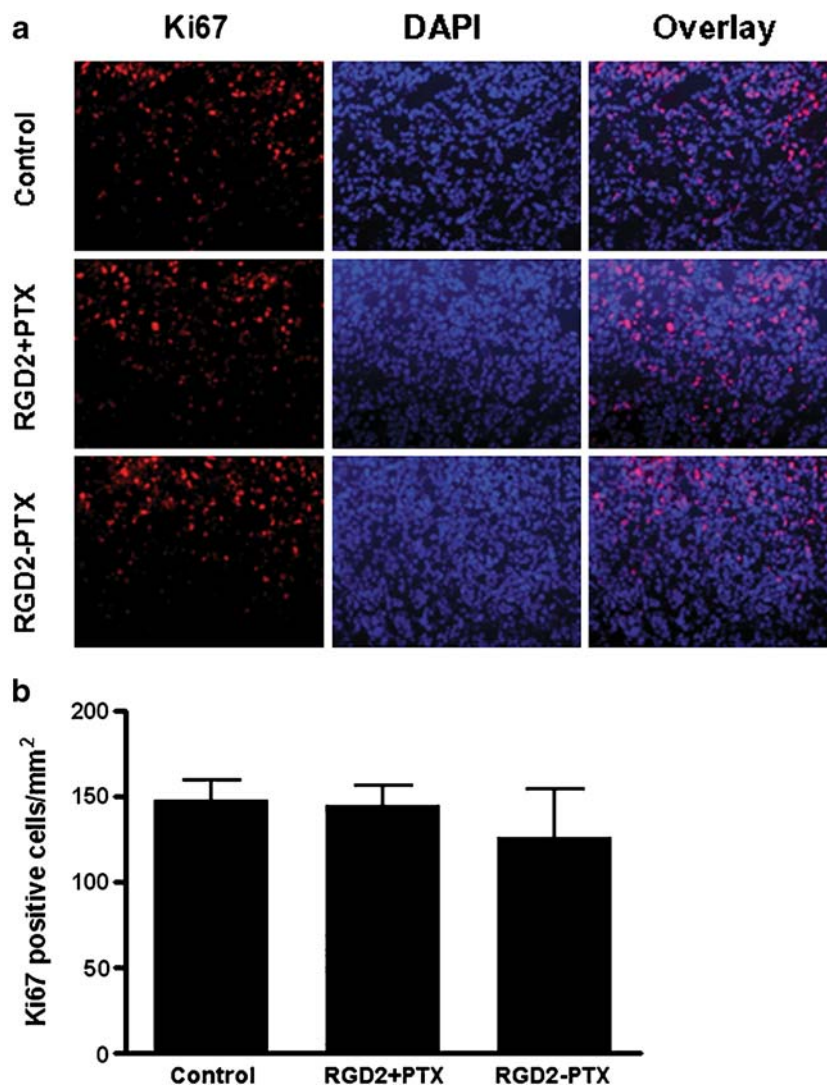
In the following experiments, tumor response to therapy was estimated by tumor volume measurement, ^{18}F-FDG PET, ^{18}F-FLT PET, and ex vivo histopathological validation. RGD2–PTX treatment showed significant tumor growth delay than the RGD2+PTX treatment group and solvent control; ^{18}F-FDG PET also revealed reduced tumor metabolism after PTX and RGD2–PTX treatment. Ex vivo immunohistochemistry revealed that RGD2–PTX is more effective than RGD2+PTX in terms of inducing tumor apoptosis and destroying tumor vasculature. However, neither ^{18}F-FLT PET nor Ki67 staining showed significant difference among the three treatment groups, which concurred with the observation that RGD2+PTX and RGD2–PTX slowed down the tumor growth, but the tumor volume still increased with time despite of multiple dose administrations. The dose and dose interval (10 mg PTX equivalent every 3 days for a total of five doses) did not seem to cause body weight loss or other visible toxicological effect. Further studies focusing on the test of the effect of various doses and treatment frequencies are required to optimize the treatment efficacy.

Despite the successful demonstration of integrin-targeted delivery of PTX for breast cancer therapy, there are several limitations to the current study. First, although ^{3}H–RGD2–PTX biodistribution showed higher tumor uptake and longer retention of PTX in the integrin-positive MDA-MB-435 tumor than PTX, the absolute tumor uptake value is still rather low, due in part to the lipophilic character of PTX and RGD2-PTX, and small molecular sizes, leading to short circulation half-life and rapid clearance. Several strategies have been employed to increase the water solubility and biocompatibility of paclitaxel. Notably, the commercial formulation of paclitaxel (i.e., Taxol®) contains Cremophor, which forms micelles that entrap the drug and increases blood half-life as compared to the DMSO formulation used in this study. More recently, a cremophor-free, albumin-stabilized formulation of paclitaxel, Abraxane®, was approved by the Food and Drug Administration for second-line therapy of advanced breast cancer. We postulate that albumin–paclitaxel conjugate with RGD peptide attachment would allow both passive targeting based on the enhanced permeability, and retention effect of tumor vasclarture and specific tumor targeting based on integrin recognition would outperform Abraxane for further enhanced anti-tumor effect of paclitaxel. Such strategy may be extended to various biocompatible nanoparticles to carry RGD peptide and PTX for controlled release therapy of cancer.

Conclusion

We have successfully demonstrated the ability of dimeric RGD peptide to deliver paclitaxel chemotherapeutic drug to integrin-positive breast cancer tumor. The treatment efficacy of RGD2–PTX was confirmed by size measurement, in vivo PET imaging, and ex vivo histopathology. The tumor growth delay is related to tumor proliferation rather than tumor metabolism as confirmed by ^{18}F-FDG/PET and ^{18}F-FLT/PET. Further improvement of the treatment efficiency and pharmacokinetics/pharmacodynamics of nanoparticle-based integrin-targeted delivery of paclitaxel is currently in progress.

References

1. McGuire WP, Rowinsky EK, Rosenshein NB, Grumbine FC, Ettinger DS, Armstrong DK, et al. Taxol: a unique antineoplastic agent with significant activity in advanced ovarian epithelial neoplasms. Ann Intern Med 1989;111:273–9.
2. Schiff PB, Fant J, Horwitz SB. Promotion of microtubule assembly in vitro by taxol. Nature 1979;277:665–7.
3. Schiff PB, Horwitz SB. Taxol stabilizes microtubules in mouse fibroblast cells. Proc Natl Acad Sci U S A 1980;77:1561–5.
4. Yvon AM, Wadsworth P, Jordan MA. Taxol suppresses dynamics of individual microtubules in living human tumor cells. Mol Biol Cell 1999;10:947–59.
5. Jordan MA, Toso RJ, Thrower D, Wilson L. Mechanism of mitotic block and inhibition of cell proliferation by taxol at low concentrations. Proc Natl Acad Sci U S A 1993;90:9552–6.
6. Eisenhauer E. Docetaxel: current status and future prospects. J Clin Oncol 1995;13:2865–8.
7. Chu Q, Vincent M, Logan D, Mackay JA, Evans WK. Taxanes as first-line therapy for advanced non-small cell lung cancer: a systematic review and practice guideline. Lung Cancer 2005;50:355–74.
8. Esteva FJ. The current status of docetaxel for metastatic breast cancer. Oncology (Williston Park) 2002;16:17–26.
9. van Hoesel QG, Verweij J, Catimel G, Clavel M, Kerbrat P, van Oosterom AT, et al. Phase II study with docetaxel (Taxotere) in advanced soft tissue sarcomas of the adult. EORTC Soft Tissue and Bone Sarcoma Group. Ann Oncol 1994;5:539–42.
10. Sharma A, Straubinger RM. Novel taxol formulations: preparation and characterization of taxol-containing liposomes. Pharm Res 1994;11:889–96.
11. Bartoli MH, Boitard M, Fessi H, Beriel H, Devissaguet JP, Picot F, et al. In vitro and in vivo antitumoral activity of free, and encapsulated taxol. J Microencapsul 1990;7:191–7.
12. Zhang X, Burt HM, Von Hoff D, Dexter D, Mangold G, Degen D, et al. An investigation of the antitumor activity and biodistribution of polymeric micellar paclitaxel. Cancer Chemother Pharmacol 1997;40:81–6.
13. Nicolaou KC, Riemer C, Kerr MA, Rideout D, Wrasidlo W. Design, synthesis and biological activity of protaxols. Nature (London, UK) 1993;364:464–6.
14. Rose WC, Clark JL, Lee FYF, Casazza AM. Preclinical antitumor activity of water-soluble paclitaxel derivatives. Cancer Chemother Pharmacol 1997;39:486–92.

15. Li C, Yu D-F, Newman RA, Cabral F, Stephens LC, Hunter N, et al. Complete regression of well-established tumors using a novel water-soluble poly(L-glutamic acid)–paclitaxel conjugate. Cancer Res 1998;58:2404–9.

16. Schally AV, Nagy A. Chemotherapy targeted to cancers through tumoral hormone receptors. Trends Endocrinol Metab 2004;15:300–10.

17. Chen X, Plasencia C, Hou Y, Neamati N. Synthesis and biological evaluation of dimeric RGD peptide-paclitaxel conjugate as a model for integrin-targeted drug delivery. J Med Chem 2005;48:1098–106.

18. Cheng YF, Kramer RH. Human microvascular endothelial cells express integrin-related complexes that mediate adhesion to the extracellular matrix. J Cell Physiol. 1989;139:275–86.

19. Temming K, Schiffelers RM, Molema G, Kok RJ. RGD-based strategies for selective delivery of therapeutics and imaging agents to the tumour vasculature. Drug Resist Updat. 2005;8:381–402.

20. Deutsch HM, Glinski JA, Hernandez M, Haugwitz RD, Narayanan VL, Suffness M, et al. Synthesis of congeners and prodrugs. 3. Water-soluble prodrugs of taxol with potent antitumor activity. J Med Chem 1989;32:788–92.

21. Visvikis D, Cheze-LeRest C, Costa DC, Bomanji J, Gacinovic S, Ell PJ. Influence of OSEM and segmented attenuation correction in the calculation of standardised uptake values for [18F]FDG PET. Eur J Nucl Med 2001;28:1326–35.

22. Jacobs AH, Rueger MA, Winkeler A, Li H, Vollmar S, Waerzeggers Y, et al. Imaging-guided gene therapy of experimental gliomas. Cancer Res 2007;67:1706–15.

^{18}F-FPPRGD2 and ^{18}F-FDG PET of Response to Abraxane Therapy

Xilin Sun[1,2], Yongjun Yan[1], Shuanglong Liu[3], Qizhen Cao[3], Min Yang[1], Nouri Neamati[4], Baozhong Shen[2], Gang Niu[1,5], and Xiaoyuan Chen[1]

[1]Laboratory of Molecular Imaging and Nanomedicine, National Institute of Biomedical Imaging and Bioengineering, National Institutes of Health, Bethesda, Maryland; [2]Department of Medical Imaging and Nuclear Medicine, the 4th Affiliated Hospital, Harbin Medical University, Harbin, China; [3]Molecular Imaging Program at Stanford (MIPS), Department of Radiology, Stanford University School of Medicine, Stanford, California; [4]School of Pharmacy, University of Southern California, Los Angeles, California; and [5]Imaging Sciences Training Program, Radiology and Imaging Sciences, Clinical Center, National Institute of Biomedical Imaging and Bioengineering, National Institutes of Health, Bethesda, Maryland

Abraxane (nanoparticle albumin-bound paclitaxel) is an anticancer drug approved by the Food and Drug Administration. However, the mechanism of action of Abraxane is complex, and no established biomarker is available to accurately monitor its treatment outcomes. The aim of this study was to investigate whether the integrin-specific PET tracer ^{18}F-FPPRGD2 (investigational new drug 104150) can be used to monitor early response of tumors to Abraxane therapy. **Methods:** Orthotopic MDA-MB-435 breast cancer mice were treated with Abraxane (25 mg/kg every other day, 3 doses) or phosphate-buffered saline. Tumor volume was monitored by caliper measurement. PET scans were obtained before and at different times after the start of treatment (days 0, 3, 7, 14, and 21) using ^{18}F-FPPRGD2 and ^{18}F-FDG. The tumoricidal effect was also assessed ex vivo by immunohistochemistry. **Results:** Abraxane treatment inhibited the tumor growth, and a significant difference in tumor volume could be seen at day 5 after the initiation of treatment. The tumor uptake of ^{18}F-FPPRGD2 in the Abraxane-treated group was significantly lower on days 3 and 7 than at baseline but returned to the baseline level at days 14 and 21, indicative of relapse of the tumors after the treatment was halted. Immunohistologic staining confirmed that the change of ^{18}F-FPPRGD2 uptake correlated with the variation of integrin level in the tumor vasculature induced by Abraxane treatment. No significant change of tumor (rather than vascular) integrin expression was observed throughout the study. No significant decrease of ^{18}F-FDG uptake was found between the treated and the control tumors on days 3, 14, and 21, although an increase in ^{18}F-FDG tumor uptake of treated mice, as compared with the control mice, was found on day 7. The increase of ^{18}F-FDG on day 7 was related to the inflammatory response during therapy. **Conclusion:** Abraxane-mediated downregulation of integrin $\alpha_v\beta_3$ expression on tumor endothelial cells can be quantitatively visualized by PET. The change of integrin expression precedes that of tumor size. Consequently, ^{18}F-FPPRGD2 PET is superior to ^{18}F-FDG PET in monitoring early response to treatment, favoring its potential clinical translation.

Key Words: therapy response; positron emission tomography (PET); Abraxane; ^{18}F-FDG; RGD

P aclitaxel was originally derived from the bark of the Pacific Yew tree in the early 1960s. It can disrupt microtubule reorganization and lead to G2/M cell cycle arrest (*1*). As a potent cytotoxic agent, paclitaxel is widely used against various refractory and metastatic malignancies (*2,3*). However, it is also well known for its ability to produce hypersensitivity reactions and its limited aqueous solubility (*4,5*). The clinical use of paclitaxel has been improved significantly by formulating this drug in polyethoxylated castor oil–free, albumin-bound, 130-nm particles named Abraxane (nanoparticle albumin-bound paclitaxel; Abraxis BioScience).

Abraxane is an important therapeutic breakthrough, because it addresses the toxicities associated with solvents in taxane-based chemotherapy and minimizes the occurrence of severe anaphylactic reactions (*6,7*). In addition, compared with paclitaxel, Abraxane can improve drug delivery into the tumor (*8,9*). The antiangiogenesis activity of paclitaxel has been observed even at low concentrations, which did not affect cellular microtubule assembly (*10,11*). Paclitaxel also showed an inhibitory effect on the growth of transplanted human oral squamous cell carcinoma and reduced the expression of vascular endothelial growth factor (VEGF) and CD31 (*12*). However, contradictory reports also exist that Abraxane triggers reactionary angiogenesis by upregulating VEGF-A expression in a breast cancer model (*2*).

Integrins are composed of a family of heterodimeric glycoproteins responsible for the regulation of cellular

activation, migration, proliferation, survival, and differentiation (*13*). One of the most important members of this receptor class is integrin $\alpha_v\beta_3$, which is preferentially expressed on several types of cancer cells, including melanoma, glioma, and ovarian and breast cancers (*14*). Integrin $\alpha_v\beta_3$ is also expressed on proliferating endothelial cells associated with neovascularization in both malignant tumors and normal tissue but not in quiescent blood vessels (*15,16*).

Because peptides containing arginine-glycine-aspartic acid (RGD) can bind strongly to integrin $\alpha_v\beta_3$, many RGD peptide probes have been developed for multimodality imaging of integrin expression (*17–21*). Targeting the $\alpha_v\beta_3$ integrin receptor could provide us with a tool to visualize and quantify integrin $\alpha_v\beta_3$ expression levels; early cellular and molecular effects of therapies (especially on vascular modulation), without having to rely on invasive histologic staining; consequential changes in blood perfusion and permeability; and terminal morphologic changes, such as substantial tumor mass or volume reduction (*14*).

^{18}F-FPPRGD2 is an ^{18}F-labeled dimeric RGD peptide recently developed in our laboratory that has higher receptor binding affinity than monomeric RGD peptide counterparts and enhanced tumor uptake (*22*). An exploratory investigative new drug application (IND 104150) for ^{18}F-FPPRGD2 was recently approved by the Food and Drug Administration for the first tests in humans. In this study, we performed longitudinal PET studies to compare the abilities of ^{18}F-FPPRGD2 and ^{18}F-FDG to evaluate the treatment efficacy of Abraxane in an MDA-MB-435 human breast cancer xenograft model.

MATERIALS AND METHODS

Radiochemistry

^{18}F-FPPRGD2 was synthesized as previously reported (*22*). In brief, PEG3-E[c(RGDyK)]$_2$ (denoted as PRGD2) was added to dried 4-nitrophenyl 2-^{18}F-fluoropropionate, followed by the addition of *N,N*-diisopropylethylamine. The labeled peptide was purified by reversed-phase high-performance liquid chromatography on a semipreparative C-18 column. After trapping with a C-18 cartridge preactivated with 5 mL of ethanol and 10 mL of water, the product was washed with 2 mL of water and eluted with 2 mL of ethanol. After the ethanol solution was blown dry with a slow stream of N_2 at 60°C, the ^{18}F-labeled peptide was redissolved in phosphate-buffered saline (PBS) solution and passed through a 0.22-μm Millipore filter into a sterile multidose vial for in vivo experiments. Radiochemical yield was approximately 95%. The specific activity was approximately 37 TBq/mmol.

Preparation of MDA-MB-435 Breast Cancer Model

The MDA-MB-435 human breast carcinoma tumor model known to express medium levels of integrin $\alpha_v\beta_3$ (*23*) was used for the in vivo imaging studies. The MDA-MB-435 cell line was purchased from American Type Culture Collection and grown in Leibovitz's L-15 medium supplemented with 10% (v/v) fetal bovine serum under a 100% air atmosphere at 37°C. The MDA-MB-435 tumor model was generated by orthotopic injection of 5×10^6 cells in the left mammary fat pad of female athymic nude mice (Harlan Laboratories). The mice were used for studies when the

tumor volume reached about 250 mm^3 ($\sim$10–14 d after implantation). Tumor growth was followed by caliper measurements of perpendicular diameters of the tumor. The tumor volume was estimated by the formula tumor volume = a × (b^2)/2, where a and b were the tumor length and width, respectively, in millimeters. All animal experiments were performed in compliance with the guidelines for the care and use of research animals established by Stanford University's Animal Studies Committee.

Longitudinal Small-Animal PET Scans

PET scans and image analysis were performed using an Inveon microPET scanner (Siemens Medical Solutions). Each MDA-MB-435 tumor–bearing mouse was injected via the tail vein with 3.7 MBq (100 μCi) of ^{18}F-FPPRGD2 or 7.4 MBq (200 μCi) of ^{18}F-FDG under isoflurane anesthesia. Five-minute static scans were acquired at 1 h after injection. For the ^{18}F-FDG scan, mice were maintained under isoflurane anesthesia during the injection, accumulation, and scanning periods and were kept fasting for 4 h before tracer injection. For the ^{18}F-FPPRGD2 scan, mice were not anesthetized during the tracer accumulation period and were not kept fasting before tracer injection. The images were reconstructed and quantified using procedures described in the supplemental materials (supplemental materials are available online only at http://jnm.snmjournals.org).

As shown in Table 1, 40 mice underwent baseline PET with ^{18}F-FPPRGD2 (*n* = 20) or ^{18}F-FDG (*n* = 20) (day 0) when the tumors reached a size of around 250 mm^3. Then the tumor-bearing mice were randomly divided into the following 4 groups (*n* = 10/group): ^{18}F-FPPRGD2 control, ^{18}F-FPPRGD2 treatment, ^{18}F-FDG control, and ^{18}F-FDG treatment. Mice in the treatment groups received 3 doses of Abraxane diluted in PBS, and control mice received PBS only. Doses of Abraxane (25 mg/kg) or PBS were administered on days 0, 2, and 4. PET scans were repeated on days 3, 7, 14, and 21. At each time point, 1 mouse from each group was sacrificed, and the tumors were excised for histopathology.

Fluorescence Staining

Frozen tumor tissue slices (8 μm) were fixed with cold acetone for 20 min and dried in the air for 30 min at room temperature. After blocking with 1% bovine serum albumin for 30 min, the sections were incubated with humanized antihuman integrin $\alpha_v\beta_3$ antibody Abegrin (*24*) (20 μg/mL) for 1 h at room temperature and

TABLE 1
Experimental Design for Longitudinal ^{18}F-FDG and ^{18}F-FPPRGD2 Imaging of Abraxane Treatment Efficacy and Ex Vivo Histopathology

Parameter	0	2	3	4	7	14	21
^{18}F-FPPRGD2							
Control	#, +	+	#	+	#	#	#
Abraxane	#, +	+	#	+	#	#	#
^{18}F-FDG							
Control	#, +	+	#	+	#	#	#
Abraxane	#, +	+	#	+	#	#	#
Histology	−		−		−		−

= small-animal PET; + = PBS or Abraxane treatment; − = tumor tissue sampling.

then visualized with cy3-conjugated donkey antihuman secondary antibodies (1:300; Jackson ImmunoResearch Laboratories). For the overlay staining of CD31 and CD61, slices were incubated with rat antimouse CD31 antibody (1:200; BD Biosciences) and hamster anti-β3 CD61 antibody (1:200; BD Biosciences) and then visualized with cy3-conjugated goat antirat and fluorescein isothiocyanate–conjugated goat antihamster secondary antibody (1:300; Jackson ImmunoResearch Laboratories). For the overlay staining of Ki67 and F4/80, slices were incubated with rabbit antimouse Ki76 antibody (1:200; BD Biosciences) and rat antimouse F4/80 antibody (1:200; Abcam, Inc.) and then visualized with cy3-conjugated goat antirabbit and fluorescein isothiocyanate–conjugated goat antirat secondary antibody (1:300; Jackson ImmunoResearch Laboratories). After being washed 5 times with PBS, the slices were mounted with 4′-6-diamidino-2-phenylindole (DAPI)-containing mounting medium and observed under an epifluorescence microscope (X81; Olympus). Each experiment was performed in pairs, and the pairs were then repeated twice.

Statistical Analysis

Quantitative data were expressed as means ± SD. Means were compared using 1-way ANOVA and a Student t test. P values less than 0.05 were considered statistically significant. Unpaired Student t tests were used to evaluate differences between the 2 treatment groups, and paired Student t tests were performed for differences between time points on the activity curve within a treatment condition.

RESULTS

Abraxane Treatment–Inhibited MDA-MB-435 Tumor Growth

Abraxane is effective in delaying MDA-MB-435 tumor growth. Intravenous administration of 3 doses of Abraxane (25 mg/kg; days 0, 2, and 4) resulted in a reduction in tumor volume. As shown in Figure 1A, a time-related increase in tumor volume was observed in the PBS control group, in which the tumors showed an average fractional tumor volume (V/V_0) of 1.27, 1.42, 1.51, 1.78, and 2.63 on days 3, 5, 7, 14, and 21, respectively. Abraxane treatment resulted in a V/V_0 of 0.99, 0.78, 0.67, 0.51, and 0.65 on days 3, 5, 7, 14, and 21, respectively. The average tumor size of the control group became significantly smaller than that of the treatment group starting from day 5 ($P < 0.05$). In the treated mice, an increase of fractional tumor volume from day 14 ($V/V_0 = 0.51$) to day 21 ($V/V_0 = 0.65$) was noted. This pattern of initial response during and immediately after the treatment, and then regrowth after the treatment was stopped, is common in many other experimental cancer therapy studies and clinical cancer trials (25–27). Mouse body weight was monitored as an indicator of the toxicity of Abraxane. As evidenced in Figure 1B, it is clear that Abraxane had no observable side effects at the low dosage used in this study.

PET with ^{18}F-FPPRGD2 and ^{18}F-FDG

Static PET images at 1 h after injection of ^{18}F-FDG (Fig. 2) or ^{18}F-FPPRGD2 (Fig. 3) were acquired at day 0 (baseline, before Abraxane treatment) and at days 3, 7, 14, and
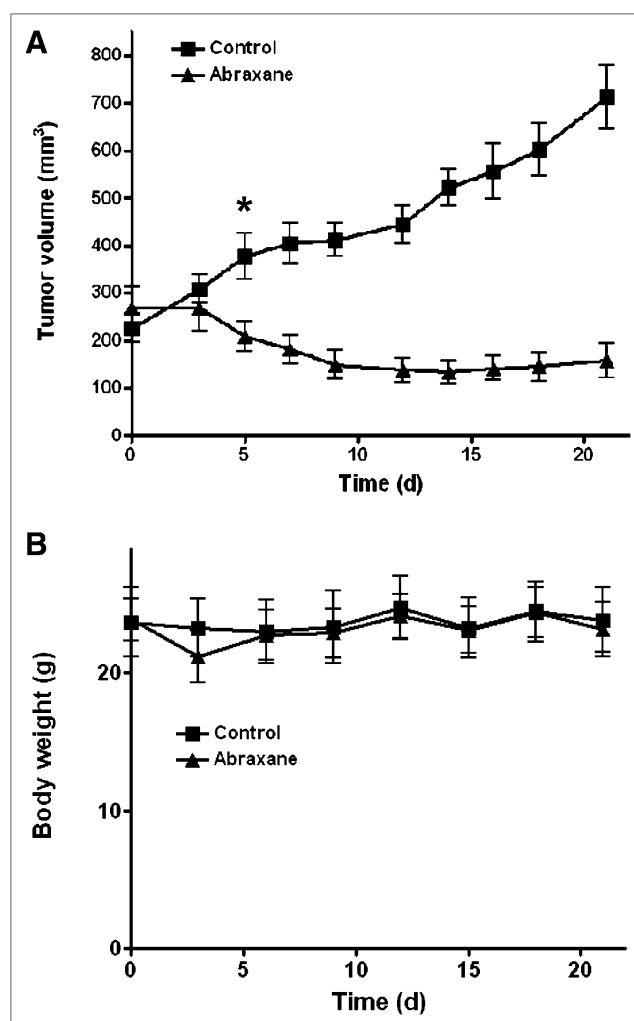

FIGURE 1. Antitumor activity of Abraxane in established MDA-MB-435 xenografts. (A) 3 doses of Abraxane (intravenous injection, 25 mg/kg/dose on days 0, 2, and 4) led to substantial tumor regression but also regrowth after day 14. (B) Body weight of animals treated with PBS or Abraxane.

21 after the Abraxane treatment was initiated. The tumor region-of-interest analysis is summarized in Figure 4. As shown in Figures 2 and 4A, there was little fluctuation of ^{18}F-FDG uptake in the control mice at different days after tumor inoculation. Abraxane treatment led to some increase of ^{18}F-FDG uptake at days 3 and 7, which returned to the baseline level at days 14 and 21. Figures 3 and 4B describe the tumor uptake pattern of ^{18}F-FPPRGD2 with and without Abraxane treatment. After Abraxane treatment, the MDA-MB-435 tumor uptake of ^{18}F-FPPRGD2 significantly decreased from 1.22 ± 0.08 percentage injected dose per gram (%ID/g) (day 0) to 1.08 ± 0.10 %ID/g (day 3, $P < 0.05$) and 0.63 ± 0.06 %ID/g (day 7, $P < 0.01$), which represents a decrease of up to 48%. At days 14 and 21, the ^{18}F-FPPRGD2 in the treated mice increased to the level in the control mice, with tumor uptake of 1.42 ± 0.14 and 1.23 ± 0.19 %ID/g, respectively.
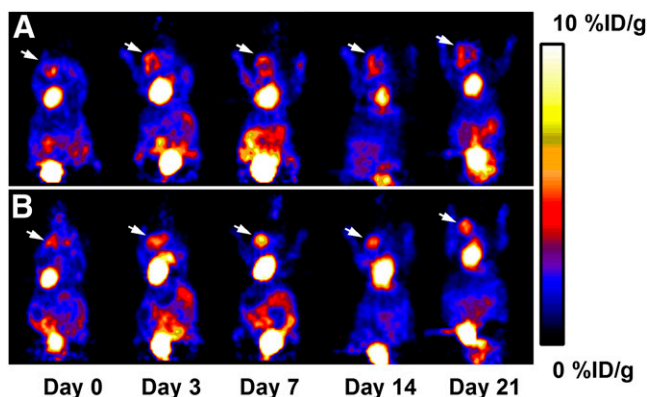
FIGURE 2. Representative decay-corrected whole-body coronal images of female athymic nude mice bearing orthotopic MDA-MB-435 tumors at 1 h after intravenous injection of ^{18}F-FDG (7.4 MBq/mouse) on days 0, 3, 7, 14, and 21 after treatment was initiated. Increased uptake of ^{18}F-FDG was observed on days 3 and 7, decreasing to baseline level on days 14 and 21. (A) PBS control. (B) Abraxane treatment.

Abraxane-Induced Inflammation and Inhibition of Proliferation

To evaluate the therapeutic effect of Abraxane on MDA-MB-435 tumors, we performed Ki67 immunofluorescence staining on tumor sections. The percentage of Ki67-positive cells (Ki67 staining index) in untreated tumors was around 72% ± 17%, independent of the tumor size (Fig. 5). Consistent with the tumor growth inhibition, significantly delayed cell proliferation was observed in the Abraxane-treated mice at days 3 and 7 with a Ki67 SI of 17% ± 7% and 22% ± 5%, respectively ($P < 0.01$) (Supplemental Fig. 1). The Ki67 SI was restored to the baseline level at days 14 and 21.

The tumor sections were also stained against macrophage-specific marker F4/80 to evaluate Abraxane-induced inflammation. Compared with control tumors, a more pronounced inflammatory reaction was observed at days 3 and 7 after
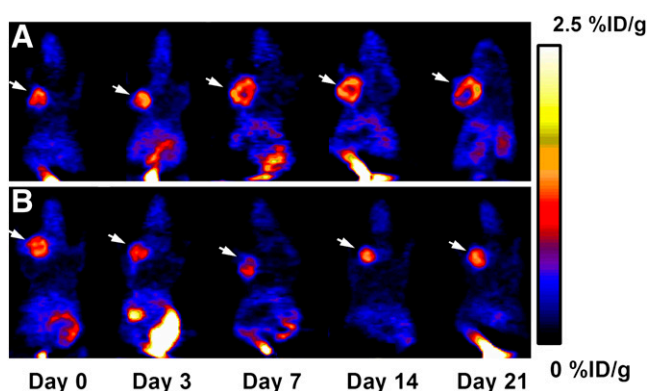

FIGURE 3. Representative decay-corrected whole-body coronal images of female athymic nude mice bearing orthotopic MDA-MB-435 tumors at 1 h after intravenous injection of ^{18}F-FPPRGD2 (3.7 MBq/mouse) on days 0, 3, 7, 14, and 21 after treatment was initiated. Decreased tumor uptake of ^{18}F-FPPRGD2 was observed on days 3 and 7 but was restored to baseline level on days 14 and 21. (A) PBS control. (B) Abraxane treatment.
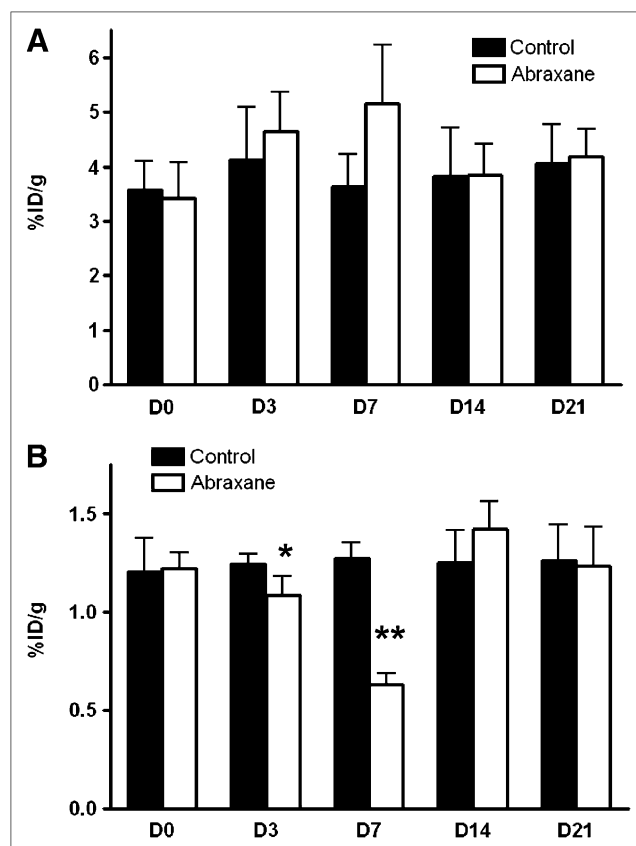

FIGURE 4. Quantitative small-animal PET region-of-interest analysis of tumor uptake for ^{18}F-FDG (A) and ^{18}F-FPPRGD2 (B).

treatment. At day 14, F4/80-positive macrophages decreased significantly ($P < 0.01$) (Supplemental Fig. 2).

Effect of Abraxane on Tumor Integrin Expression

To further investigate the mechanism of altered ^{18}F-FPPRGD2 uptake during and after Abraxane treatment, integrin expression was evaluated by immunofluorescence staining. Because integrin on tumor vascular endothelial cells was of murine origin and that on tumor cells was of human origin, we stained tumor sections with both antimurine integrin β3 and antihuman integrin $\alpha_v\beta_3$ antibodies. As shown in Figure 6A, MDA-MB-435 tumor cells had positive human integrin $\alpha_v\beta_3$ staining, which was unaffected by Abraxane treatment.

Murine β3 was colocalized with murine CD31, indicating that the expression of murine integrin β3 was mainly on the tumor vascular endothelial cells. A significant morphologic change of tumor vasculature, including the collapse of microvessel cavities, was observed in Abraxane-treated tumors at different times. In addition, after Image J (National Institutes of Health) analysis, we found that the mean murine β3 fluorescence intensity decreased significantly at days 3 ($P < 0.05$) and 7 ($P < 0.01$) (Supplemental Fig. 3) after Abraxane treatment; the treated tumors and control tumors had similar vascular integrin levels at days 14 and 21, correlating with the ^{18}F-FPPRGD2 imaging studies.
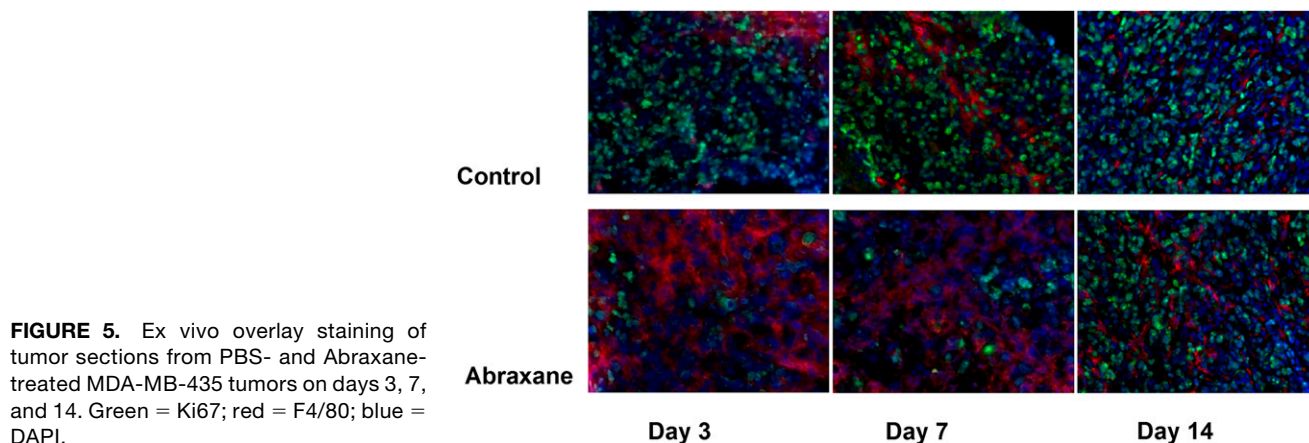
FIGURE 5. Ex vivo overlay staining of tumor sections from PBS- and Abraxane-treated MDA-MB-435 tumors on days 3, 7, and 14. Green = Ki67; red = F4/80; blue = DAPI.

DISCUSSION

The ability to visualize and quantify integrin $\alpha_v\beta_3$ expression levels noninvasively in vivo provides new opportunities to document integrin expression, greatly assist the understanding of mechanisms of angiogenesis and antiangiogenic treatment, and monitor treatment efficacy. We have previously reported a series of radiolabeled RGD monomers and multimers for imaging integrin $\alpha_v\beta_3$ expression (18,22,28–32). Among them, ^{18}F-FPPRGD2, with relatively high tumor

integrin-specific accumulation and favorable in vivo kinetics, has made its way into the clinic for cancer diagnosis and for treatment response monitoring (22).

There have been several studies using suitably labeled monomeric RGD peptide tracers to monitor chemotherapy or antiangiogenic treatment efficacy. For example, paclitaxel therapy in Lewis lung carcinoma tumor–bearing mice significantly retarded tumor growth and was accompanied by a corresponding reduction of tumor glucosamino ^{99m}Tc-D-c(RGDfK) uptake, as determined by γ-camera imaging,
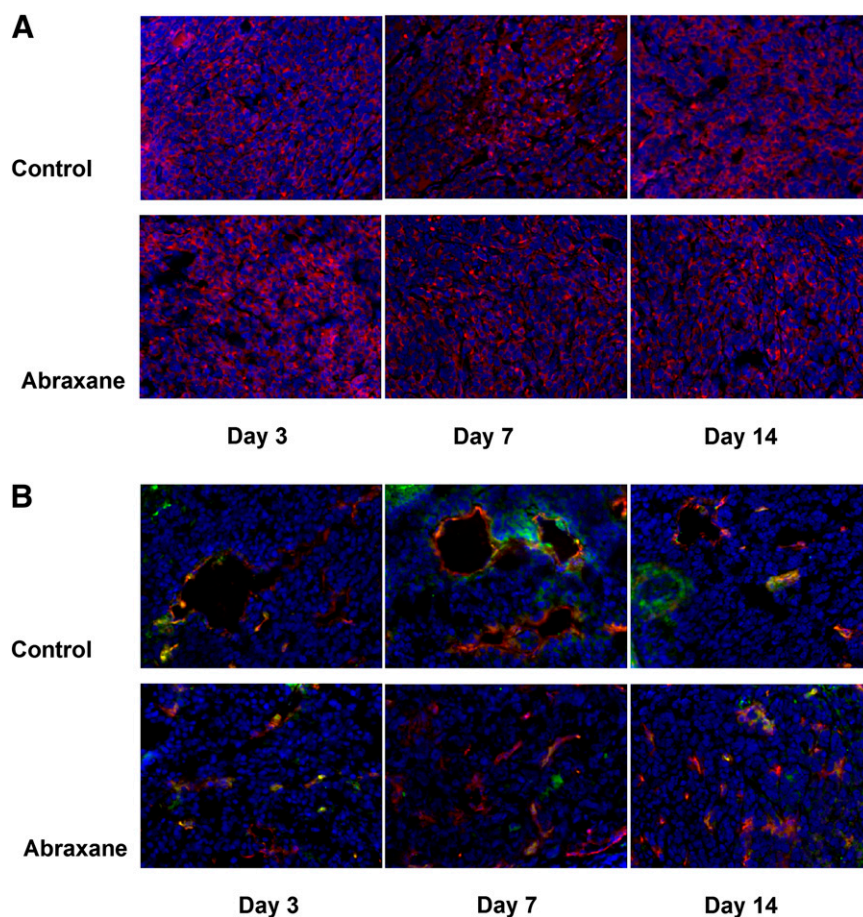

FIGURE 6. (A) Ex vivo human integrin staining of tumor sections from PBS- and Abraxane-treated MDA-MB-435 tumors on days 3, 7, and 14. (B) Overlay staining of CD31 (red), murine integrin β3 (green), and DAPI (blue) of tumor sections from PBS- and Abraxane-treated MDA-MB-435 tumors on days 3, 7, and 14.

correlating well with tumor α_v integrin expression levels (*33*). Similarly, paclitaxel therapy reduced the microvessel density in Lewis lung carcinoma tumor–bearing mice and resulted in significantly reduced tumor uptake of ^{18}F-AH111585. ZD4190 (a small-molecular-weight VEGF receptor-2 tyrosine kinase inhibitor) therapy resulted in a significant decrease in ^{18}F-AH111585 uptake in Calu-6 tumors, compared with vehicle control-treated Calu-6 tumors (*34*). Dasatinib, an Src-family kinase inhibitor, reduced ^{64}Cu-DOTA-c(RGDfK) uptake in a U87MG xenograft model. In contrast, tumor ^{18}F-FDG uptake showed no significant reduction with dasatinib therapy (*35*). All these studies supported the feasibility of noninvasive imaging using RGD-based probes to monitor antiangiogenic therapy response.

In this study, we investigated the potential of ^{18}F-FPPRGD2 to accurately assess therapeutic response of human mammary carcinomas to Abraxane treatment and to be translated into the clinic for integrin $\alpha_v\beta_3$ imaging. In vivo small-animal PET showed that there was a significant reduction in the tumor uptake of ^{18}F-FFPPRGD2 as early as day 3 after the initiation of Abraxane treatment. Moreover, this reduction in tumor accumulation of ^{18}F-FPPRGD2 was observed before a tumor size decrease could be discerned by caliper measurement, suggesting that ^{18}F-FPPRGD2 can detect early responses preceding clinical regression. We also performed a comparison study with ^{18}F-FDG as an imaging tracer. ^{18}F-FDG showed increased tumor uptake at days 3 and 7, despite positive tumor response to Abraxane treatment.

It is worth mentioning that our longitudinal scans showed an initial decrease and subsequent restoration of ^{18}F-FPPRGD2 after Abraxane treatment, as is consistent with the pattern of initial growth inhibition and tumor relapse after treatment is stopped. However, the change of ^{18}F-FPPRGD2 uptake accurately predicted the tumor response a few days before the anatomic tumor size change could be accurately measured. Immunohistochemical staining also confirmed that the change of ^{18}F-FPPRGD2 uptake reflected tumor vascular integrin level, rather than tumor cell integrin expression (which was unaffected by Abraxane treatment). The exact mechanism by which Abraxane affects the vascular integrin but not tumor cell integrin expression is not well understood and will be a subject of future studies.

Despite the cytoxicity of Abraxane, ^{18}F-FDG uptake was somewhat increased at the early stage of treatment, possibly because of the combined effect of reduced tumor cell proliferation (Ki67 index) and increased macrophage infiltration (F4/80 staining) in regressing tumors. It has been well documented that ^{18}F-FDG can show high uptake when inflammatory cells are present (*36,37*)—which is the potential limitation of ^{18}F-FDG when used to monitor therapeutic response. ^{18}F-FPPRGD2 is superior to ^{18}F-FDG, because the uptake of ^{18}F-FPPRGD2 seems not to be influenced by tumor-associated macrophages after therapy. Thus, it can identify MDA-MB-435 tumor response to Abraxane more accurately.

The promising imaging results elucidated in this longitudinal study suggest the usefulness of quantitative ^{18}F-FPPRGD2 PET to evaluate treatments that produce an antiangiogenic effect and a change in vascular integrin level. However, we have to bear in mind that tumor uptake and accumulation of a given radiotracer are not solely dependent on receptor expression. Several other factors, including vascular density and volume, vascular permeability, and interstitial fluid pressure, also affect the distribution (*38,39*). To explore the usefulness of ^{18}F-FPPRGD2 in monitoring treatment response, studies in various tumor models with different integrin $\alpha_v\beta_3$ expression patterns and different sensitivities to certain therapeutics should be conducted. In certain cases, receptor binding potential derived from dynamic scans, instead of tumor uptake or tumor-to-background ratio, might be needed to eliminate the influence of tumor microenvironment on the pharmacokinetics of ^{18}F-FPPRGD2. ^{18}F-FPPRGD2 alone or in combination with additional functional imaging modalities can enhance our mechanistic understanding of how novel molecular therapeutic strategies affect tumors and allow early prediction of treatment efficacy and potential relapse, leading to better individualization of chemotherapy.

CONCLUSION

Our data illustrate that ^{18}F-FPPRGD2 is a promising PET tracer that allows noninvasive evaluation of response to treatments that affect integrin $\alpha_v\beta_3$ level, before size changes can be found. It also has the potential to provide earlier clinical opportunities to adjust anticancer drug doses and intervals to maintain sustained antitumor effect and avoid relapse. ^{18}F-FPPRGD2 is superior to ^{18}F-FDG in monitoring anticancer treatment, because ^{18}F-FPPRGD2 imaging is not significantly affected by the presence of infiltrating macrophages in regressing tumors.

ACKNOWLEDGMENTS

REFERENCES

1. Li CJ, Li YZ, Pinto AV, Pardee AB. Potent inhibition of tumor survival in vivo by beta-lapachone plus taxol: combining drugs imposes different artificial checkpoints. *Proc Natl Acad Sci USA.* 1999;96:13369–13374.
2. Volk LD, Flister MJ, Bivens CM, et al. Nab-paclitaxel efficacy in the orthotopic model of human breast cancer is significantly enhanced by concurrent anti-vascular endothelial growth factor A therapy. *Neoplasia.* 2008;10:613–623.
3. Damascelli B, Cantu G, Mattavelli F, et al. Intraarterial chemotherapy with polyoxyethylated castor oil free paclitaxel, incorporated in albumin nanoparticles (ABI-007): phase II study of patients with squamous cell carcinoma of the head and neck and anal canal—preliminary evidence of clinical activity. *Cancer.* 2001;92:2592–2602.
4. Rodriguez-Antona C. Pharmacogenomics of paclitaxel. *Pharmacogenomics.* 2010;11:621–623.

5. Singh S, Dash AK. Paclitaxel in cancer treatment: perspectives and prospects of its delivery challenges. *Crit Rev Ther Drug Carrier Syst.* 2009;26:333–372.

6. Desai N, Trieu V, Yao Z, et al. Increased antitumor activity, intratumor paclitaxel concentrations, and endothelial cell transport of cremophor-free, albumin-bound paclitaxel, ABI-007, compared with cremophor-based paclitaxel. *Clin Cancer Res.* 2006;12:1317–1324.

7. Gradishar WJ, Tjulandin S, Davidson N, et al. Phase III trial of nanoparticle albumin-bound paclitaxel compared with polyethylated castor oil-based paclitaxel in women with breast cancer. *J Clin Oncol.* 2005;23:7794–7803.

8. Petrelli F, Borgonovo K, Barni S. Targeted delivery for breast cancer therapy: the history of nanoparticle-albumin-bound paclitaxel. *Expert Opin Pharmacother.* 2010;11:1413–1432.

9. Link JS, Waisman JR, Nguyen B, Jacobs CI. Bevacizumab and albumin-bound paclitaxel treatment in metastatic breast cancer. *Clin Breast Cancer.* 2007;7:779–783.

10. Belotti D, Vergani V, Drudis T, et al. The microtubule-affecting drug paclitaxel has antiangiogenic activity. *Clin Cancer Res.* 1996;2:1843–1849.

11. Wang J, Lou P, Lesniewski R, Henkin J. Paclitaxel at ultra low concentrations inhibits angiogenesis without affecting cellular microtubule assembly. *Anticancer Drugs.* 2003;14:13–19.

12. Myoung H, Hong SD, Kim YY, Hong SP, Kim MJ. Evaluation of the anti-tumor and anti-angiogenic effect of paclitaxel and thalidomide on the xenotransplanted oral squamous cell carcinoma. *Cancer Lett.* 2001;163:191–200.

13. Ruegg C, Alghisi GC. Vascular integrins: therapeutic and imaging targets of tumor angiogenesis. *Recent Results Cancer Res.* 2010;180:83–101.

14. Desgrosellier JS, Cheresh DA. Integrins in cancer: biological implications and therapeutic opportunities. *Nat Rev Cancer.* 2010;10:9–22.

15. Kassmeyer S, Plendl J, Custodis P, Bahramsoltani M. New insights in vascular development: vasculogenesis and endothelial progenitor cells. *Anat Histol Embryol.* 2009;38:1–11.

16. Weis SM. Evaluating integrin function in models of angiogenesis and vascular permeability. *Methods Enzymol.* 2007;426:505–528.

17. Cai W, Chen X. Multimodality molecular imaging of tumor angiogenesis. *J Nucl Med.* 2008;49(suppl 2):113S–128S.

18. Chen X. Multimodality imaging of tumor integrin αvβ3 expression. *Mini Rev Med Chem.* 2006;6:227–234.

19. Liu Z, Li ZB, Cao Q, Liu S, Wang F, Chen X. Small-animal PET of tumors with ^{64}Cu-labeled RGD-bombesin heterodimer. *J Nucl Med.* 2009;50:1168–1177.

20. Dimastromatteo J, Riou LM, Ahmadi M, et al. In vivo molecular imaging of myocardial angiogenesis using the αvβ3 integrin-targeted tracer ^{99m}Tc-RAFT-RGD. *J Nucl Cardiol.* 2010;17:435–443.

21. Myers TA, Kaushal D, Philipp MT. Microglia are mediators of Borrelia burgdorferi-induced apoptosis in SH-SY5Y neuronal cells. *PLoS Pathog.* 2009;5:e1000659.

22. Liu S, Liu Z, Chen K, et al. ^{18}F-labeled galacto and PEGylated RGD dimers for PET imaging of αvβ3 integrin expression. *Mol Imaging Biol.* 2010;12:530–538.

23. Zhang X, Xiong Z, Wu Y, et al. Quantitative PET imaging of tumor integrin αvβ3 expression with ^{18}F-FRGD2. *J Nucl Med.* 2006;47:113–121.

24. Liu Z, Jia B, Zhao H, Chen X, Wang F. Specific targeting of human integrin αvβ3 with ^{111}In-labeled abegrin in nude mouse models. *Mol Imaging Biol.* April 10, 2010 [Epub ahead of print].

25. Cao Q, Li ZB, Chen K, et al. Evaluation of biodistribution and anti-tumor effect of a dimeric RGD peptide-paclitaxel conjugate in mice with breast cancer. *Eur J Nucl Med Mol Imaging.* 2008;35:1489–1498.

26. Wang H, Chen K, Cai W, et al. Integrin-targeted imaging and therapy with RGD4C-TNF fusion protein. *Mol Cancer Ther.* 2008;7:1044–1053.

27. Niu G, Chen X. Has molecular and cellular imaging enhanced drug discovery and drug development? *Drugs R D.* 2008;9:351–368.

28. Shi J, Kim YS, Zhai S, Liu Z, Chen X, Liu S. Improving tumor uptake and pharmacokinetics of ^{64}Cu-labeled cyclic RGD peptide dimers with Gly$_3$ and PEG$_4$ linkers. *Bioconjug Chem.* 2009;20:750–759.

29. Liu Z, Niu G, Shi J, Liu S, Wang F, Chen X. ^{68}Ga-labeled cyclic RGD dimers with Gly3 and PEG4 linkers: promising agents for tumor integrin αvβ3 PET imaging. *Eur J Nucl Med Mol Imaging.* 2009;36:947–957.

30. Li ZB, Cai W, Cao Q, et al. ^{64}Cu-labeled tetrameric and octameric RGD peptides for small-animal PET of tumor αvβ3 integrin expression. *J Nucl Med.* 2007;48:1162–1171.

31. Wu Z, Li ZB, Chen K, et al. microPET of tumor integrin αvβ3 expression using ^{18}F-labeled PEGylated tetrameric RGD peptide (^{18}F-FPRGD4). *J Nucl Med.* 2007;48:1536–1544.

32. Cai W, Niu G, Chen X. Imaging of integrins as biomarkers for tumor angiogenesis. *Curr Pharm Des.* 2008;14:2943–2973.

33. Jung KH, Lee KH, Paik JY, et al. Favorable biokinetic and tumor-targeting properties of ^{99m}Tc-labeled glucosamino RGD and effect of paclitaxel therapy. *J Nucl Med.* 2006;47:2000–2007.

34. Morrison MS, Ricketts SA, Barnett J, Cuthbertson A, Tessier J, Wedge SR. Use of a novel Arg-Gly-Asp radioligand, ^{18}F-AH111585, to determine changes in tumor vascularity after antitumor therapy. *J Nucl Med.* 2009;50:116–122.

35. Dumont RA, Hildebrandt I, Su H, et al. Noninvasive imaging of αvβ3 function as a predictor of the antimigratory and antiproliferative effects of dasatinib. *Cancer Res.* 2009;69:3173–3179.

36. Avril N, Menzel M, Dose J, et al. Glucose metabolism of breast cancer assessed by ^{18}F-FDG PET: histologic and immunohistochemical tissue analysis. *J Nucl Med.* 2001;42:9–16.

37. Kubota R, Yamada S, Kubota K, Ishiwata K, Tamahashi N, Ido T. Intratumoral distribution of fluorine-18-fluorodeoxyglucose in vivo: high accumulation in macrophages and granulation tissues studied by microautoradiography. *J Nucl Med.* 1992;33:1972–1980.

38. Niu G, Li Z, Xie J, Le QT, Chen X. PET of EGFR antibody distribution in head and neck squamous cell carcinoma models. *J Nucl Med.* 2009;50:1116–1123.

39. Niu G, Sun X, Cao Q, et al. Cetuximab-based immunotherapy and radioimmunotherapy of head and neck squamous cell carcinoma. *Clin Cancer Res.* 2010;16:2095–2105.

ness, are now being raised as arguments against randomised trials of diagnostic techniques" (8). This still applies (at least partly) in 2012. However, as with RCTs in drug interventions, we expect that the value of RCTs in diagnostic imaging in general and in PET in particular will be increasingly acknowledged. In the meantime we are looking forward to an objective and "evidence-based" discussion on this issue.

REFERENCES

1. Bossuyt PM, McCaffery K. Additional patient outcomes and pathways in evaluations of testing. *Med Decis Making*. 2009;29:E30–E38.
2. Buyse M, Michiels S, Sargent DJ, Grothey A, Matheson A, de Gramont A. Integrating biomarkers in clinical trials. *Expert Rev Mol Diagn*. 2011;11:171–182.
3. Ferrante di Ruffano L, Hyde CJ, McCaffery KJ, Bossuyt PM, Deeks JJ. Assessing the value of diagnostic tests: a framework for designing and evaluating trials. *BMJ*. 2012;344:e686.
4. Lijmer JG, Bossuyt PM. Various randomized designs can be used to evaluate medical tests. *J Clin Epidemiol*. 2009;62:364–373.
5. Sargent DJ, Conley BA, Allegra C, Collette L. Clinical trial designs for predictive marker validation in cancer treatment trials. *J Clin Oncol*. 2005;23:2020–2027.
6. Schünemann HJ, Oxman AD, Brozek J, et al. Grading quality of evidence and strength of recommendations for diagnostic tests and strategies. *BMJ*. 2008; 336:1106–1110.
7. Valk PE. Do we need randomised trials to evaluate diagnostic procedures? Against. *Eur J Nucl Med Mol Imaging*. 2004;31:132–135.
8. Van Tinteren H, Hoekstra OS, Boers M. Do we need randomised trials to evaluate diagnostic procedures? For. *Eur J Nucl Med Mol Imaging*. 2004;31:129–131.
9. Brush J, Boyd K, Chappell F, et al. The value of FDG positron emission tomography/computerised tomography (PET/CT) in pre-operative staging of colorectal cancer: a systematic review and economic evaluation. *Health Technol Assess*. 2011;15:1–192.
10. Ruers TJ, Wiering B, van der Sijp JR, et al. Improved selection of patients for hepatic surgery of colorectal liver metastases with ^{18}F-FDG PET: a randomized study. *J Nucl Med*. 2009;50:1036–1041.
11. Picardi M, De Renzo A, Pane F, et al. Randomized comparison of consolidation radiation versus observation in bulky Hodgkin's lymphoma with post-chemotherapy negative positron emission tomography scans. *Leuk Lymphoma*. 2007;48:1721–1727.
12. Altman DG, Bland JM. Absence of evidence is not evidence of absence. *BMJ*. 1995;311:485.
13. Viney RC, Boyer MJ, King MT, et al. Randomized controlled trial of the role of positron emission tomography in the management of stage I and II non-small-cell lung cancer. *J Clin Oncol*. 2004;22:2357–2362.
14. Higgins JPT, Green S. Cochrane handbook for systematic reviews of interventions, version 5.1.0. Available at: www.cochrane-handbook.org. Accessed September 27, 2012.
15. Black N. Why we need observational studies to evaluate the effectiveness of health care. *BMJ*. 1996;312:1215–1218.
16. Plewnia C, Reimold M, Najib A, Reischl G, Plontke SK, Gerloff C. Moderate therapeutic efficacy of positron emission tomography-navigated repetitive transcranial magnetic stimulation for chronic tinnitus: a randomised, controlled pilot study. *J Neurol Neurosurg Psychiatry*. 2007;78:152–156.
17. Freeman PR. The performance of the two-stage analysis of two-treatment, two-period crossover trials. *Stat Med*. 1989;8:1421–1432.

Fülöp Scheibler*
Polina Zumbé
Inger Janssen
Melanie Viebahn
Milly Schröer-Günther
Robert Grosselfinger
Elke Hausner
Stefan Sauerland
Stefan Lange
Institute for Quality and Efficiency in Health Care
Dillenburger Strasse 27
Cologne 51105, Germany
E-mail: fueloep.scheibler@iqwig.de

Erratum

There were some errors in the Acknowledgments section of "[18]F-FPPRGD2 and ^{18}F-FDG PET of Response to Abraxane Therapy," by Sun et al. (*J Nucl Med*. 2011;52:140–146). The corrected Acknowledgments appear below. The authors regret the error.